DISSERTAÇÃO DE MESTRADO Nº 1058

HARMONIC CURRENT COMPENSATION APPLIED IN SINGLE-PHASE PHOTOVOLTAIC SYSTEMS

Lucas Santana Xavier

DATA DA DEFESA: 15/06/2018

Universidade Federal de Minas Gerais

Escola de Engenharia

Programa de Pós-Graduação em Engenharia Elétrica

HARMONIC CURRENT COMPENSATION APPLIED IN SINGLE-PHASE PHOTOVOLTAIC SYSTEMS

Lucas Santana Xavier

Dissertação de Mestrado submetida à Banca Examinadora designada pelo Colegiado do Programa de Pós-Graduação em Engenharia Elétrica da Escola de Engenharia da Universidade Federal de Minas Gerais, como requisito para obtenção do Título de Mestre em Engenharia Elétrica.

Orientador: Prof. Victor Flores Mendes

Belo Horizonte - MG

Junho de 2018

Xavier, Lucas Santana.
X3h Harmonic current compensation applied to single-phase photovoltaic systems [manuscrito] / Lucas Santana Xavier. - 2018.
xxi, 80 f., enc.: il.

Orientador: Victor Flores Mendes.
Coorientador: Heverton Augusto Pereira.

Dissertação (mestrado) Universidade Federal de Minas Gerais, Escola de Engenharia.

Bibliografia: f. 75-80.

1. Engenharia elétrica - Teses. 2. Geração de energia fotovoltaica - Teses. 3. Potência reativa (Engenharia elétrica) - Teses. I. Mendes, Victor Flores. II. Pereira, Heverton Augusto. III. Universidade Federal de Minas Gerais. Escola de Engenharia. IV. Título.

CDU: 621.3(043)

À minha família,
mentores e amigos.

"Entender é transformar o que existe."

Jiddu Krishnamurti

Agradecimentos

Primeiramente, agradeço aos meus pais, Maurício e Beatriz, e aos meus irmãos, Marina e Daniel, por terem me dado todo apoio que precisei, devo tudo a eles. Agradeço a Ana Carolina de Oliveira pelo companheirismo, me apoiando muito nessa jornada.

Agradeço aos professores Victor Flores Mendes, Heverton Augusto Pereira e Allan Fagner Cupertino pela paciência e pelo imenso conhecimento científico e de vida que obtive durante esses anos.

Agradeço aos amigos e companheiros de laboratŕio, que deram muito suporte: Victor Magno, Marcos, Valmor. Aos amigos de república André Badaia, Thiago, João, Jose, Rafael, Herbert. Obrigado aos integrantes do GESEP e a todos aos meus amigos.

Agradeço aos professores do Programa de Pós-Graduação em Engenharia Elétrica pelos valiosos conhecimentos que irei levar durante minha vida profissional e transmiti-los também.

Agradeço a UFMG e ao LCCE/CPH por fornecer a estrutura e equipamentos necessários para a execução deste trabalho. Agradeço a UFV, onde me formei em Engenharia Elétrica.

Summary

Resumo

A geração fotovoltaica tem crescido em todo o mundo, principalmente na geração distribuída. A possibilidade de gerar energia elétrica próximo aos centros urbanos pode reduzir os impactos de longas linhas de transmissão e diversificar a matriz energética de um país. A principal função do inversor fotovoltaico é injetar a energia gerada pela planta solar na rede. Entretanto, durante variações da irradiância solar, os inversores fotovoltaicos tem uma margem de corrente que não é explorada. Por isso, trabalhos na literatura tem proposto serviços auxiliares realizados por inversores fotovoltaicos. Esse conceito é baseado em adicionar outras funções à estratégia de controle convencional, tais como injeção de potência reativa e compensação de corrente harmônica. Entretanto, um importante fato e pouco relatado na literatura é sobre técnicas para compensar parcialmente corrente harmônica de modo a garantir que o inversor opere abaixo de sua corrente máxima estabelecida. Portanto, este trabalho propõe estratégias de compensação seletiva e parcial de corrente harmônica. Um método de detecção de corrente harmônica adaptativo de modo a realizar a compensação seletiva de corrente harmônica e duas estratégias de limitação de corrente harmônica para compensação parcial de harmônicos são introduzidos. Estudos de caso em ambiente de simulação e experimental são abordados para validar a performace das estratégias propostas neste trabalho. Resultados mostram uma melhoria na qualidade de energia da rede através da compensação de corrente harmônica, sem sobrecarregar o inversor fotovoltaico.

Palavras-chaves: Serviços Auxiliares, Geração Distribuída, Compensação de Corrente Harmônica, Limitação de Corrente do Inversor, Sistemas Fotovoltaicos.

Abstract

The photovoltaic power generation have been rising around the world, especially in the distributed generation. The possibility to generate energy in proximity of consumer units can reduce the impacts of long transmission lines and diversify the energy matrix of a country. The main function of the photovoltaic inverter is to inject the power generated by the solar plant into the electrical grid. However, due to variations in solar irradiance, inverters have a current margin which is not explored during the day. Hence, some works have addressed the ancillary services provided by photovoltaic inverters. This concept is based on adding other functions to the conventional control strategy, such as reactive power injection and harmonic current compensation. However, an important fact and less related in literature is about techniques to compensate partially harmonic current in order to ensure that the inverter works below its rated current. Thereby, this work proposes strategies of selective and partial harmonic current compensation. An adaptive harmonic current detection method in order to perform the selective harmonic current compensation and two harmonic current limitation strategies for partial harmonic compensation are introduced. Case studies in simulation and experimental environment are addressed to validate the performance of the strategies proposed here. The results show an improvement in the grid power quality through harmonic current compensation, without overloading the photovoltaic inverter.

Keywords: Ancillary Services, Distributed Generation, Harmonic Current Compensation, Inverter Current Limitation, Photovoltaic Systems.

List of Tables

List of Figures

Symbol List

C_{pv}	Photovoltaic array output capacitance
C_{dc}	DC-link capacitance
L_b	Boost converter inductance
L_i	Inverter side inductance of the LCL filter
L_g	Grid side inductance of the LCL filter
L_f	Equivalent inductance of the inverter filter
R_b	Equivalent series resistance of the boost converter inductor
R_f	Equivalent series resistance of the inverter filter
R_S	Series resistance of the photovoltaic array
R_P	Parallel resistance of the photovoltaic array
R_{mpp}	Output Resistance of the photovoltaic array at the maximum power point
i_{pv}	Current generated by photovoltaic array
i_s	Inverter current
i_s^*	Inverter current reference
i_g	Grid current
i_L	Load current and boost inductor current
$\tilde{i}_L$	Harmonic current
i_o	Leakage current of the photovoltaic array model
i_{sc}	Short-circuit current of the photovoltaic panel
i_{mpp}	Maximum power point current of the photovoltaic panel
I_h	Harmonic current amplitude
I_f	Fundamental current amplitude
I_m	Peak value of the inverter current reference
I_m^*	Inverter rated current

I_α	Fundamental component contribution to the inverter current peak value
I_L	Harmonic component contribution to the inverter peak value
v_{pv}	Photovoltaic string output voltage
v_{dc}	DC-link voltage
v_g	Grid voltage
v_t	Panel thermal voltage of the photovoltaic array model
v_{oc}	Open-circuit voltage of the photovoltaic panel
v_{mpp}	Voltage at maximum power point of the photovoltaic panel
d	Duty cycle of the boost converter
ω_o	Initial angular frequency of the harmonic current detector
ω_n	PLL Natural angular frequency
ω_h	Harmonic angular frequency
ω_f	Fundamental angular frequency
f_f	Fundamental frequency
f_s	switching frequency
f_n	PLL natural frequency
f_{cf}	Cut-off frequencies of the low-pass filter
f_{ca}	Cut-off frequencies of the low-pass filter
t	Time
T_s	Sampling period
T_o	Half period of the fundamental period
ζ	PLL Damping factor
k	SOGI gain
K_h	Harmonic compensation factor
W	Energy
Q	Reactive power
Q^*	Reactive power reference injected by photovoltaic system
P	Active power
P^*	Active power reference injected by photovoltaic system
P_{mp}	Maximum power of the photovoltaic array
S	Apparent power
S^*	Apparent power reference injected by photovoltaic system
Sm	Inverter rated Apparent power
n_s	Number of cells in series
a	Diode ideality constant of the photovoltaic array model
k	Boltzmann constant
T	Temperature of the photovoltaic panel
G	Solar Irradiance
K_v	Temperature coefficient of the photovoltaic array model
K_i	Temperature coefficient of the photovoltaic array model

$K_{p_{bi}}$	Proportional gain of the inner loop of the boost converter control
$K_{i_{bi}}$	Integral gain of the inner loop of the boost converter control
$K_{p_{bv}}$	Proportional gain of the outer loop of the boost converter control
$K_{i_{bv}}$	Integral gain of the outer loop of the boost converter control
$K_{p,pll}$	Proportional gain of the PLL control
$K_{i,pll}$	Integral gain of the PLL control
K_p	Proportional gain of the multi-resonant controller
K_{ih}	Resonant gains of the multi-resonant controller
$K_{p_{sv}}$	Proportional gain of the v_{dc}^2 control based method
$K_{i_{sv}}$	Integral gain of the v_{dc}^2 control based method
$K_{p,sat}$	Proportional gain of the current limitation strategy based on closed-loop
$K_{i,sat}$	Integral gain of the current limitation strategy based on closed-loop

Superscripts

$*$	Reference value

Subscribers

α	quantities referred to the stationary reference-frame
β	quantities referred to the stationary reference-frame
d	quantities referred to the synchronous reference-frame
q	quantities referred to the synchronous reference-frame

List of Acronyms

ANEEL	*Agência Nacional de Energia Elétrica*
DG	Distributed Generation
ICMS	*Imposto Sobre Circulação de Mercadorias e Serviços*
PV	Photovoltaic
DC	Direct Current
AC	Alternating Current
MPPT	Maximum Power Point Tracking
MPP	Maximum Power Point
P&O	Perturbation and Observation
PI	Proportional and Integral
PCC	Point of Common Coupling

THD	Total Harmonic Distortion
TDD	Total Demand Distortion
SRF-PLL	Syncronous Reference Frame-Phase-locked loop
SOGI	Second Order Generalized Integrator
PMR	Proportional Multi-Resonant
RPC	Repetitive Controller
FLL	Frequency Locked Loop
DFT	Discrete Fourier Transform
LPF	Low-Pass Filter
RMS	Root Mean Square
CCVT	Current Contribution Value Tracking
HCL	Harmonic Current Limitation
HC	Harmonic Compensation

Chapter 1

Introduction

Brazil has structured its power generation system based on hydraulic power plants since the end of the 19th century, when the first hydroelectric power plant started to operate in Diamantina (CEMIG, 2012). The importance of the hydroelectric power plants in the structural change and economic development of the Brazil in the last 100 years is evident. On the other hand, the Brazilian electrical power system became very dependent on this type of resource.

Since 2011, Brazil is facing an intense water scarcity in several regions, including places where important hydroelectric power stations are installed. As results, thermoelectric power plants are increasing the generation capacity with concern to save water in hydroelectric stations reservoirs (PINTO et al., 2015). However, the generated electric energy based on thermoelectric power plants is at least twice as expensive as based on hydraulic processes, besides injecting greenhouse gases into the atmosphere.

It is a consensus that Brazil has diversified its electric energy sources in the last 15 years. However, data from 2018 show that hydraulic generation accounts for 60.7% of supply, as shown in Fig. 1.1 (ANEEL, 2018). The solar, wind and biomass sources are only responsible for 0.75%, 7.7% and 8.7% of supply, respectively, although the data shows that Brazil presents an electricity matrix predominantly renewable. Although most economic indicators appoint that renewable energy sources may occupy a significant share of the world's energy matrix, the projections for installations in Brazil are far below when compared with countries such as China, Germany, United States, Japan, Indian and other countries (REN21, 2017).

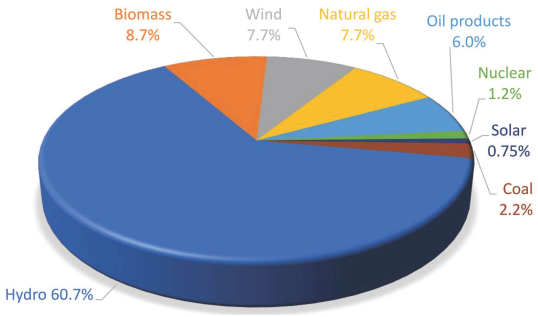

Figure 1.1: Electricity supply by resource in Brazil (year 2018) (ANEEL, 2018).

1.1 The Distributed Generation

An interesting possibility to diversify a country energy matrix is through Distributed Generation (DG). This expression is used to appoint the electric power generation near to energy consumers, avoiding long transmission lines. However, the installation of hydroelectric and thermoelectric power near to urban centers may not be viable for economic and environmental reasons. This fact has driven the use of others power generation sources in the DG, such as photovoltaic (PV) solar energy.

In 2017, photovoltaic solar systems reached 99% of the total number of installations classified as distributed micro and mini-generation (ANEEL, 2017). In terms of installed power, the PV systems reached 80.7 MW followed by wind systems with 10.2 MW. The predominance of the PV systems in the DG is due to the costs that become more attractive, besides the easy installation of solar panels on roofs and facades (ABINEE, 2012).

A landmark for distributed micro and mini-generation in Brazil was achieved with normative resolution 482/2012, published by Brazilian electricity regulatory agency ANEEL (*Agência Nacional de Energia Elétrica*), which establishes the general conditions to access the power distribution systems (ANEEL, 2012). Since then, this standard has been updated in order to make the procedures for connection of the distributed generators less bureaucratic. The main points of this standard are clarify the obligations of utilities and establishing the power compensation system, according to which eventual excesses of production in relation to consumption are transformed into credits (kWh) that can be used by the consumers on the following bills

up to (60 months ahead).

Brazil has extended the economic incentives for PV installations in the last years. Most Brazilian states have already exempt the tax on circulation of goods and transportation and communication services ICMS (*Imposto Sobre Circulação de Mercadorias e Serviços*) from photovoltaic systems. In addition, national banks are providing credit line for the PV sector. These incentives are very favorable to the energy consumers who want to have their DG. However, from the point of view of utilities, the growth of PV system in distributed micro and mini-generation is being seen as a threat, mainly due to the following factors (ABINEE, 2012):

- Possible revenue loss of companies due to the energy consumers growth using the power compensation system;
- The solar energy is a non-dispatchable source of electricity. Thus, it can not turn the solar panels on the same way that can ramp up central coal and hydro plants to match power demand.

These challenges are common in countries that have experienced the expansion of renewable energy sources in their electrical power systems. For example, Germany's biggest power companies, which were based on the electricity generation from nuclear, coal and oil sources became unprofitable with the expansion of solar and wind power in the country. To overcome this drawback, most of them were split into two companies, one for renewable energy and new services and one for conventional energy. In addition, most of these utilities mainly invest in renewable abroad. These strategies were adopted by the Germany's energy firms to survive in the new energy scenario (MORRIS; PEHNT, 2012).

The currently generation systems are balanced with the demand. This energy production mode is not compatible with the photovoltaic generation. Thus, several energy storage solutions are being studied and tested to overcome this challenge such as underground compressed air in natural caverns to pumped storage, flywheels, and batteries, in order to have a flexible system of energy production (MORRIS; PEHNT, 2012).

Despite all these challenges, PV systems can contribute for a smarter electrical system. For long time, PV installations were only considered as

active power generators. However, this perception has been changing. In fact, these systems can contribute to the grid operation through ancillary services and this will be discussed in this work.

1.2 PV Systems with Ancillary Services

The discussion about the potential to use the DG to provided ancillary services has intensified from the early 2000s due mainly to the technological advances in electrical and mechanical power conversion systems (JOOS et al., 2000), (PEPERMANS et al., 2005). At the same time, the IEEE Standard 1547 was raised for interconnecting distributed resources with electric power systems. This standard also defines the ancillary services in distributed power generation systems such as load regulation, energy losses, spinning and non-spinning reserves, voltage regulation, and reactive-power supply. The number of PV plants connected to low-voltage distribution lines has been increasing in the later years. Hence, the use of the PV systems to perform ancillary services have attracted attention from researchers (MASTROMAURO et al., 2009), (YANG, 2014).

These ancillary services that PV systems can performed are still being ignored or poorly detailed by most grid codes. However, in a wide-scale penetration scenario of PV systems in the distributed grid, the effects of intermittent power generation of this source can not be ignored. Thus, countries grid codes should be updated in the near future, aiming grid protection and support functionality, flexible power controllability and intelligent ancillary services (YANG, 2014). This demand reinforces the importance of research about the next generation of PV system.

In grid-connected PV systems, there are power electronic inverters injecting the energy extracted from the photovoltaic array into the alternating current (AC) grid. Today, this electronic device can be connected to the single-phase or three-phase power systems without transformers, reducing the weight and volume of the equipment (KJAER; PEDERSEN; BLAABJERG, 2005), (KEREKES et al., 2009). The single-phase PV inverters are commonly used for applications up to 7 kW. Above this value, three-phase inverters are usually recommended.

In most applications, photovoltaic inverters extract the PV panel energy and inject it into the grid, with unitary power factor. Due to solar irradiance variation, the PV inverters have a current margin that is not used over daily operation (BONALDO; PAREDES; POMILIO, 2016). To exemplify this fact, Fig. 1.2 shows a power generation curve of a real PV plant during a typical sunny day. It is possible to note that the nominal generation (1 pu) is achieved only few hours during the day, around 12 pm. Most of the time, the generation reaches fractions of the nominal power and between 6 pm and 6 am no power is generated and the PV system goes into standby mode.

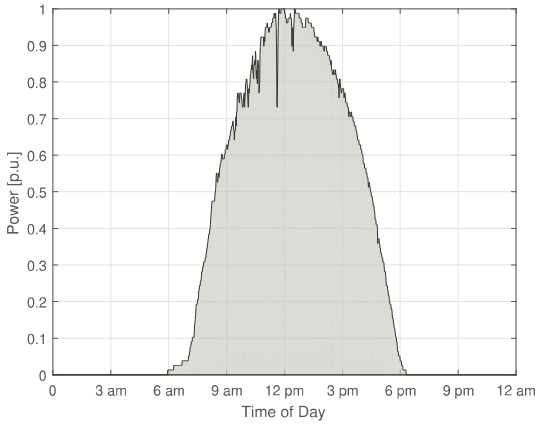

Figure 1.2: Power generation curve of a real PV plant during a day.

This fact creates an opportunity to use the PV inverters to guarantee the utility grid stability. Basically, such benefits can be achieved through the reactive power and harmonic content control in the grid.

Reactive power injection can contribute for grid voltage recovery under sags and overvoltage phenomena, thus maintaining the levels set by grid codes (MIÑAMBRES-MARCOS et al., 2015), (YANG; WANG; BLAABJERG, 2014). In addition, the PV inverters can provide the reactive power demanded by the loads connected to the point of common coupling (PCC)(CAGNANO et al., 2011).

The expansion of the electrical devices with nonlinear characteristic in the current and voltage relation have caused concerns about the proliferation of harmonics in the power system. Devices such as power electronic converters, fluorescent lamps, electronic ballasts, thyristors and computers can lead to higher harmonic current distortions which are responsible for efficiency

reduction of the power grid, besides interacting with resonances present in the system (De la Rosa, 2006). For this reason, several works have proposed to use photovoltaic systems to mitigate current and voltage harmonic distortions generated by nonlinear loads (XAVIER; CUPERTINO; PEREIRA, 2014), (BONALDO; PAREDES; POMILIO, 2016), (HE; LI; MUNIR, 2012), (PAREDES et al., 2015)

These ancillary services that PV systems can performed are still being ignored or poorly detailed by most grid codes. However, in a wide-scale penetration scenario of PV systems in the distributed grid, the effects of intermittent power generation of this source can not be ignored. Thus, countries grid codes should be updated in the near future, aiming grid protection and support functionality, flexible power controllability and intelligent ancillary services (YANG, 2014). This demand reinforces the importance of researches about the next generation of PV system.

1.3 Motivation and Objectives

Generally, the PV system sizing must be in such way that the inverter does not operate far below its rated power most of the time but also without overload conditions, in order to get the best cost and benefit of the system (PINHO; GALDINO, 2014). In such conditions, over sizing a small photovoltaic system to perform ancillary services is not a very attractive idea, once this can greatly increase the system cost.

Therefore, an interesting alternative is to maintain the sizing methodology of PV systems based on the total power of PV panels installed and use the ancillary services within this projected power range. Thus, the photovoltaic inverters act to assist the grid within their power capacity at that given moment. Two ways to perform harmonic current compensation, respecting the capacities of the PV inverter, are proposed by this work.

Firstly, the inverter switches have a current limit that cannot be exceeded, to preserve its lifetime and safety. The critical point is when harmonic current compensation is involved (PEREIRA et al., 2015). In this situation there are multiple frequencies in the current signal and analytical expressions for inverter current limitation are complex. In addition, limiting

the RMS current when there are multiple harmonic orders in the signal is not effective, since the current peak can be much larger than its RMS value. For this reason. The present work intends to scrutinize techniques to limit the peak value of the PV inverter in order to perform partial harmonic current compensation using single-phase PV systems.

Second, nonlinear load currents present several harmonic components and compensate all these components can exceed the physical and control capability of the PV inverter (LASCU et al., 2009). For this reason, this work intends to scrutinize a method for selective harmonic current compensation, where only some predominant harmonics are detected and compensated.

1.4 Methodology

The methodology to achieve these goals is:

- Mathematical modeling in time and frequency domain in order to describe parameters for the method and techniques proposed in this work and for the PV system control;
- Simulation results in PLECS environment using computational model presenting relevant dynamics of the PV system;
- Experimental validation of the proposed method and techniques through a prototype system built in the laboratory.

1.5 Contributions

In view of the above discussions, the main contributions of this work are:

- Propose a harmonic current detection method to perform selective harmonic current compensation;
- Propose harmonic current limitation techniques for partial harmonic current compensation by reducing the PV inverter current peak.

The results produced in this work originated two conference papers and one paper in a journal. They are cited below per chronological order:

- L. S. Xavier, A. F. Cupertino, V. F. Mendes and H. A. Pereira, "Detection method for multi-harmonic current compensation applied in three-phase photovoltaic inverters," 12th IEEE International Conference on Industry Applications (INDUSCON), Curitiba, 2016, pp. 1-8.

- L. S. Xavier, A. F. Cupertino, J. T. de Resende, V. F. Mendes, H. A. Pereira, "Adaptive current control strategy for harmonic compensation in single-phase solar inverters, Electric Power Systems Research, vol. 142, 2017, pp. 84-95.

- L. S. Xavier, V. M. R. de Jesus, A. F. Cupertino, V. F. Mendes and H. A. Pereira, "Novel adaptive saturation scheme for photovoltaic inverters with ancillary service capability," 8th International Symposium on Power Electronics for Distributed Generation Systems (PEDG), Florianopolis, 2017, pp. 1-8.

The published conference papers in correlated topics are cited below per chronological order:

- V. M. R. de Jesus, L. S. Xavier, A. F. Cupertino, H. A. Pereira and V. F. Mendes, "Comparison of MPPT strategies applied in three-phase photovoltaic inverters during harmonic current compensation", 12th IEEE International Conference on Industry Applications (INDUSCON), Curitiba, 2016, pp. 1-8.

- V. M. R. de Jesus, L. S. Xavier, A. F. Cupertino, V. F. Mendes and H. A. Pereira. Operating limits of three-phase multifunctional photovoltaic converters applied for harmonic current compensation, 8th International Symposium on Power Electronics for Distributed Generation Systems (PEDG), Florianopolis, 2017, pp. 1-8.

1.6 Text Organization

In this first chapter an overview of the use of PV system in DG was presented and several ancillary services were briefly described. The motivation and objectives of this work were clarified, as well as the methodology used in order to reach these aims. Finally, the intended contributions were set.

The second chapter describes the main control structures used in this work. The mathematical model of each structure are presented as well.

In the third chapter, a harmonic current detection method is proposed for selective harmonic current compensation. In fourth chapter, techniques for partial harmonic current compensation are introduced.

In the last chapter the conclusions are presented and the proposals for continuation are listed.

Chapter 2

Single-Phase PV System with Ancillary Services

In this chapter, an overview on the basic and advanced functions of the single-phase PV system is described and presented in Fig. 2.1.

In addition to the basic functions, the focus is the harmonic current compensation and the reactive power injection. Fig. 2.1 shows that the system connection for basic and advanced functions are similar. However, to include in the PV inverters the capability to perform reactive power injection and harmonic current compensation, additional current sensor is necessary to detect the load current, mainly if the control strategy is performed by current controllers. For these purposes, the load current information is taken from the sum between the grid current and the inverter current. This ensures that the current information of all loads connected to the PCC is achieved.

2.1 Photovoltaic Array Modelling

The devices responsible for photovoltaic conversion are solar cells. These structures can be represented as a diode with its p-n junction exposed to irradiance (RAUSCHENBACH, 1980). The typical PV silicon cells can generate power ranging from 1 W to 2 W, approximately. Thereby, in practical and commercial applications, solar cells are associated in series or parallel, forming the PV modules.

The ideal PV cell can be represented by a direct current source (i_{pv}) in

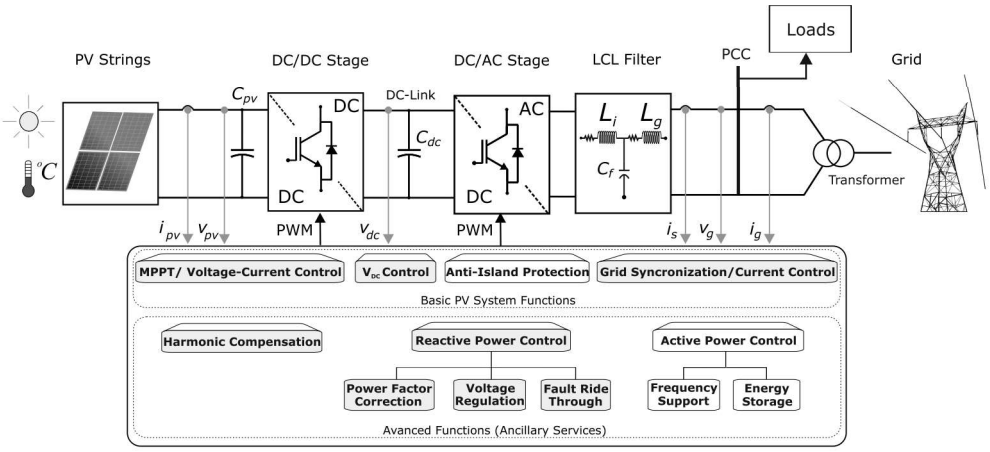

Figure 2.1: Generic scheme of the grid-connected photovoltaic system for single-phase applications.

parallel with the diode. This representation describes the I-V characteristics of an ideal PV cell. However, the equivalent series (R_S) and parallel resistances (R_P) are added to increase the accuracy of the PV array model. These resistances depend on the contact resistance of the metal base with the semiconductor layers and on the leakage current of the p-n junction.

A PV array can be represented by the electrical equivalent circuit shown in Fig. 2.2. Thereby, from the semiconductor physics, the generated current from the PV cell terminals (i) can be represented by the following expression (RAUSCHENBACH, 1980):

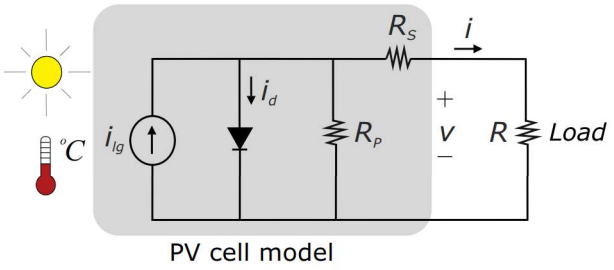

Figure 2.2: Electrical model of solar cell.

$$i = i_{lg} - i_0 \left[\exp\left(\frac{v + R_s i}{v_t a} \right) - 1 \right] - \frac{v + R_s i}{R_p}, \tag{2.1}$$

where i_{lg} is the light-generated current, i_0 is the leakage current of the diode, a is the diode ideality constant, v_t is the panel thermal voltage, which is defined as:

$$v_t = \frac{n_s k T}{q}, \tag{2.2}$$

where n_s is the number of cells connected in series, k is the Boltzmann constant ($1.3806503 \times 10^{-23}\ J/K$), $T[K]$ is the temperature of the p-n junction and q is the elementary charge ($1.60217646 \times 10^{-19}\ C$).

The light-generated current is directly proportional to the irradiance $G[W/m^2]$ and changes linearly with the temperature, as shown in the following expression:

$$i_{lg} = [i_{lg_n} + K_i(T - T_n)]\,\frac{G}{G_n}, \tag{2.3}$$

where i_{lg_n} is the photo-generated current at nominal conditions of solar irradiance (G_n) and temperature (T_n), generally 25 ^oC and 1000 W/m^2. K_i is the temperature coefficient of the short-circuit current. Generally, the datasheets provide the nominal short-circuit current (i_{scn}), thus i_{lg_n} can be expressed as:

$$i_{lg_n} = \frac{R_P + R_S}{R_P} i_{scn}. \tag{2.4}$$

The diode leakage current (i_o) can be represented by (VILLALVA; GAZOLI; FILHO, 2009):

$$i_0 = \frac{i_{scn} + K_i(T - T_n)}{\exp\left[\frac{v_{ocn} + K_v(T - T_n)}{a v_t}\right] - 1}, \tag{2.5}$$

where K_v is the temperature coefficient of the open-circuit voltage.

The influence of the R_P and R_S resistances is higher when the device operates in the current source region or in the voltage source region, respectively. In this work, these resistances can be found by an algorithm proposed in Villalva, Gazoli and Filho (2009), where R_S and R_P are varied until the

maximum power calculated by the solar panel model becomes equal to the maximum power from datasheet at the maximum power point.

This mathematical model of the PV array is used in the case study simulations to validate the methodology presented in this work for partial harmonic compensation and reactive power injection using a single-phase PV system. The main parameters used in the mathematical model approach can be found in most photovoltaic panels datasheets.

In this work, a traditional commercial PV panel of 250 W is used in order to form the PV array. The parameters of this panel under standard test conditions (STC) (1000 W/m^2 and module temperature 25 $°C$,) are presented in Table 2.1. The simulated PV array is composed for 2 strings with 6 panels in series in each branch, resulting in a generated power at maximum power point equal to 3 kW.

Table 2.1: Parameters of the PV panel.

Parameter	**Value**
Maximum power (P_{mpp})	250 W
Open-circuit voltage (v_{oc})	37.5 V
Short-circuit current (i_{sc})	8.5 A
Voltage at maximum power point (v_{mpp})	31.29 V
Current at maximum power point (i_{mpp})	7.99 A
Temperature coefficient of V_{oc} (K_v)	-0.313 $\%/^oC$
Temperature coefficient of I_{sc} (K_i)	0.0043 $\%/^oC$
Number of cells in series (n_s)	60
Nominal irradiance (G_n)	1000 W/m^2
Nominal operation temperature (T_n)	320 K
Panel series resistance (R_s)	0.173900 Ω
Panel parallel resistance (R_p)	379.023365 Ω

2.2 Maximum Power Point Tracking

Since 1993, the conversion efficiency of solar irradiance in electricity through multicrystalline silicon solar cells improved from 18% to 22.3% (GREEN et al., 2018). This is not a small difference in terms of PV cells, besides, this shows that it is very difficult to increase 1% in the energy conversion efficiency even with technological advances. There are new and more efficient

PV cells technologies, such as GaInP/GaAs multijunction. However, these cells are still impractical in the market due to their high manufacturing cost.

The generated power from the solar cell depends on its temperature, the solar irradiance and the electrical characteristics of the load. For this reason, the maximum power extraction is an important issue in PV generation. This goal is achieved through the maximum power point tracking (MPPT) algorithms.

Due to low algorithm complexity and low computational power requirement, the most traditional MPPT method is the Perturbation and Observation ($P\&O$) (HUSSEIN et al., 1995). This algorithm periodically increments or decrements the solar string voltage and compares the output power with the previous value. If the delivered power is increased, the solar array voltage perturbation will continue in the same direction. When the supplied power starts to decrease, the system reaches the maximum power point (MPP) and the $P\&O$ algorithm output oscillates around that point. Other traditional MPPT algorithm is the incremental conductance based method, a specific implementation of the $P\&O$ (HUSSEIN et al., 1995). This algorithm evaluates of the incremental conductance (di/dv) in each interaction period.

However, in cases of rapidly changing atmospheric conditions, the $P\&O$ algorithm can track in the wrong direction in relation to the MPP and it can cause a reduction of efficiency. This can happen when the power variation, due to solar irradiance variation, is higher than the caused by the algorithm action. Thereby, the algorithm interprets the power variation only as an effect of its own action. Hence, dP-$P\&O$ method is proposed in literature in order to solve problems caused by the rapidly changing in irradiance (SERA et al., 2008).

To solve the $P\&O$ problem during rapidly change in the solar irradiance, the dP-$P\&O$ method determines the correct tracking by means of additional power measurement at the middle of the MPPT sampling period without any perturbation. Thereby, during rapidly change in the solar irradiance, the action of this MPPT is able to interpret correctly if the power change is caused as an effect of its own action or due to solar irradiance change (SERA et al., 2008). In this work, the dP-$P\&O$ algorithm is used.

2.3 DC/DC Stage Based on Boost Converter

The DC/DC stage converter is commonly used to boost the input voltage level of the inverter, ensuring the acceptable voltage level for startup and extending its operation range during low irradiance conditions. In single-phase systems, the use of DC/DC is even more important due to power oscillation in the 2^{nd} harmonic frequency. This power oscillation results in DC-link voltage fluctuation and reduces the efficiency of the MPPT algorithm if PV modules are connected directly to the DC-link. For this reason, it is advisable to perform the MPPT algorithm in the DC/DC stage control for single-phase applications. The boost converter is widely used for these purposes (BLAABJERG et al., 2006),(YANG; ZHOU; BLAABJERG, 2015)

The connection of the PV array to the boost converter is shown in Fig. 2.3. The PV array model is linearized around the nominal maximum power point, since the operation of the device should occur preferably around this point (VILLALVA; SIQUEIRA; RUPPERT, 2010). Therefore, the PV array can be modeled by a linear circuit composed of an equivalent voltage source (v_{mpp}) and corresponding the resistance (R_{mpp}) at MPP. The DC-link can be represented by a voltage source (v_{dc}^{*}), assuming that the voltage is already controlled by the following stage. The average values of the capacitor voltage (v_{pv}) and inductor current (i_{Lb}) over one switching period can be obtained as respectively:

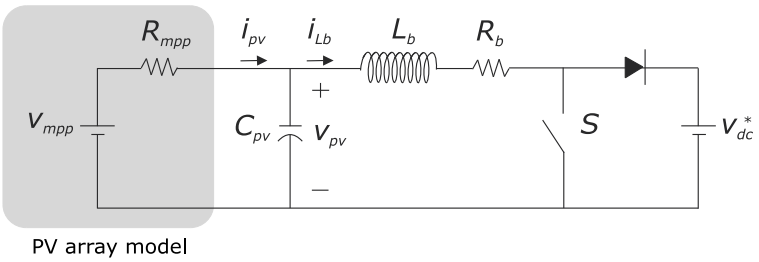

Figure 2.3: Equivalent circuit model of the DC/DC stage, PV array connected to the boost converter.

$$C_{pv}\frac{d\langle v_{pv}\rangle}{dt} = \frac{v_{mpp}}{R_{mpp}} - \frac{\langle v_{pv}\rangle}{R_{mpp}} - \langle i_{Lb}\rangle, \tag{2.6}$$

$$L_b \frac{d\langle i_{Lb}\rangle}{dt} = \langle i_L\rangle R_b + (1-d)v_{dc}^* - \langle v_{pv}\rangle, \tag{2.7}$$

where R_b is the inductor equivalent series resistance and d is the duty cycle.

The goal is to find two transfer functions in the frequency domain, relating $G_{vi}(s) = v_{pv}/i_{Lb}$ and $G_{id}(s) = i_{Lb}/d$. A small-signal approach is adopted to linearize the converter model (ERICKSON; MAKSIMOVIC, 2001). Therefore, Eq. (2.6) and (2.7) are rewritten in the frequency domain as:

$$\hat{v}_{pv}(s) = -\frac{1}{sC_{pv}R_{mpp}}\hat{v}_{pv}(s) - \frac{1}{sC_{pv}}\hat{i}_{Lb}(s), \tag{2.8}$$

$$\hat{i}_{Lb}(s) = \frac{R_b}{sL_b}\hat{i}_{Lb}(s) + \frac{v_{dc}^*}{sL_b}\hat{d}(s) - \frac{1}{sL_b}\hat{v}_{pv}(s), \tag{2.9}$$

where " ˆ " means a small-signal term. From Eq. (2.8) and (2.9) the transfer functions, which represent the relationship between G_{vi} and G_{id}, can be obtained as:

$$G_{vi}(s) = \frac{\hat{v}_{pv}}{\hat{i}_{Lb}} = -\frac{1}{sC_{pv} + \frac{1}{R_{mpp}}}, \tag{2.10}$$

$$G_{id}(s) = \frac{\hat{i}_{Lb}}{\hat{d}} = \frac{v_{dc}^*}{sL_b + R_b}, \tag{2.11}$$

Therefore, the closed-loop model of the boost converter control based on proportional-integral (PI) controllers is illustrated in Fig. 2.4. The boost converter control loop consists of an outer loop responsible for controlling the solar array output voltage (v_{pv}) and an inner loop tuned to regulate the boost converter inductor current (i_{Lb}). The voltage reference of the outer loop is calculated by the MPPT algorithm.

The proportional and integral gains of the PI controller of the inductor current control loop are adjusted by pole allocation to use the zero of the PI transfer function to cancel the G_{id} pole. Therefore, the proportional and integral gains of the inner loop are given, respectively, as:

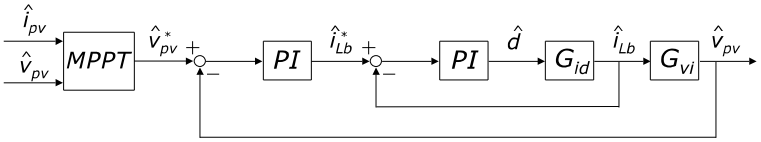

Figure 2.4: Closed-loop model of the boost converter control.

$$\begin{cases} K_{p_{bi}} = \frac{2\pi f_{ci} L_b}{v^*_{dc}}, \\ \\ K_{i_{bi}} = \frac{2\pi f_{ci} R_b}{v^*_{dc}}, \end{cases} \tag{2.12}$$

where f_{ci} is the crossover frequency of the closed-loop transfer function of the inner loop. Usually, this frequency is limited to one tenth of the maximum frequency that the actuator is capable to respond.

Similarly, the PI controller gains of the outer loop are found by pole allocation in order to use the zero of the PI transfer function to cancel the G_{vi} pole. Therefore the proportional and integral gains of the inner loop are given, respectively, as:

$$\begin{cases} K_{p_{bv}} = -2\pi f_{cv} C_{pv}, \\ \\ K_{i_{bv}} = -\frac{2\pi f_{cv}}{R_{mpp}}. \end{cases} \tag{2.13}$$

where f_{cv} is the crossover frequency of the closed-loop transfer function of the outer loop. Usually, this frequency is limited to one tenth below the frequency operation of the inner loop.

2.4 DC/AC Stage

The DC/AC stage objectives to transfer all the power extracts by the boost converter. This is achieved by controlling the DC-link voltage, keeping it higher than the grid voltage to ensure the power flow. This stage is also responsible for performing the ancillary services such as harmonic current compensation and reactive power injection.

In general, PV inverters are connected to the point of common coupling

(PCC) through passive filters to suppress the harmonic components produced during the switching process. L filters are an attractive solution due to their simple implementation (TEODORESCU; LISERRE; RODRIGUEZ, 2011). However, in practice, the connection through LCL filters has a better cost-benefit ratio due to lower volume than L filters for similar attenuation capacity. Nevertheless, LCL filters can insert resonances in the power system. Resonances can be damped through passive elements, i.e., adding a resistor in series with the filter capacitor. However, this solution reduces the PV inverter efficiency, which may have a negative impact on the market. For this reason, active damping strategies have been approached in literature (PEÑA-ALZOLA et al., 2014). This is achieved emulating the resistor action through control strategies.

In the simulation case studies the LCL filter is used to interface the PV inverter to the grid. The design procedure for the LCL filter can be found in Peña-Alzola et al. (2014). This filter design methodology taken into account the ratio between the grid and converter inductance, in order to attain low voltage drop and resonance frequency variation, achieving a very robust operation. In addition, the parameters are designed to comply with the grid connection standards in relation to the total harmonic distortion (THD) of the injected grid current and to prevent the filter capacitor to produce excessive reactive power. The LCL filter is used in the simulation case study and the L filter is employed in the experimental case study for sake of simplicity.

2.4.1 Inner Loop Control: Inverter Current Control

Fig. 2.5(a) shows a simplified scheme of the single-phase PV inverter. The LCL filter capacitor dynamics can be disregarded considering only the fundamental frequency component of the current and voltage. Applying the voltage Kirchhoff law, the average model of the grid-connected PV system can be represented as:

$$v_s - R_f i_s - L_f \frac{di_s}{dt} - v_g = 0, \tag{2.14}$$

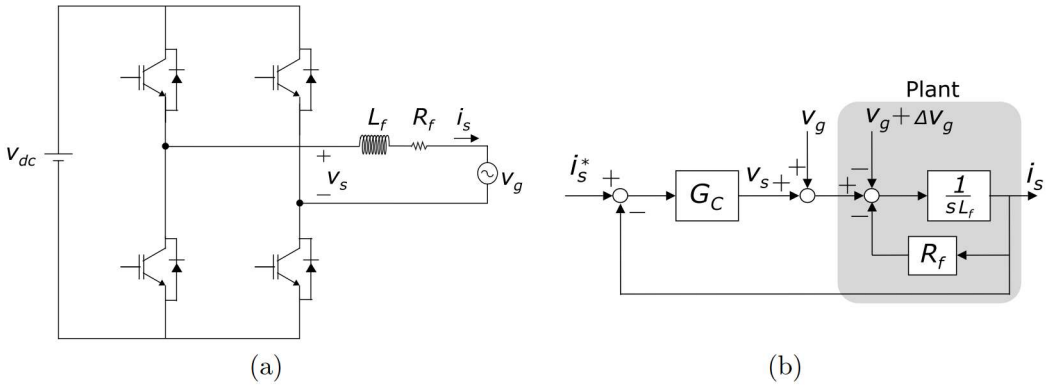

Figure 2.5: (a) Simplified illustration of the single-phase PV inverter. (b) Inverter current control model (inner loop).

where L_f and R_f are the equivalent inductance and equivalent series resistance of the filter, respectively. v_g and v_s are the grid voltage and the inverter output voltage. Through Eq. (2.14), the inverter current control in frequency domain is shown in Fig. 2.5(b), where G_c is the current controller. Note that the grid voltage is a system disturbance and its action is feedforward to the control loop in order to reduce the controller effort.

When harmonic current compensation is performed, the inverter current reference has one or more harmonic components. In this case, proportional-integral (PI) controller inserts steady state error due its limited bandwidth (CUPERTINO et al., 2013). Therefore, to overcome this drawback, resonant controllers have been employed when harmonic currents are compensated (YANG; ZHOU; BLAABJERG, 2015), (YEPES et al., 2011). The resonant controller provides a theoretical infinite gain at the resonant frequency and reduces the steady state error. However, one resonant controller needs to be designed for each compensated harmonic component. Therefore, the proportional multi-resonant controller (PMR) is used.

The PMR controller is composed for a proportional controller in parallel with resonant controllers tuned in each frequency. The PMR transfer function is given by (YEPES et al., 2011):

$$G_C(s) = K_p + \sum_{h=1}^{n} K_{ih} \overbrace{\frac{s}{s^2 + \omega_h^2}}^{R_h(s)}, \tag{2.15}$$

where K_p is the proportional gain, h is the harmonic order ($h = 1, 2, 3..., n$), ω_h are resonant frequencies and K_{ih} are the resonant gains for each harmonic frequency. The PMR controller has high gains at its resonant frequencies. Thereby, the term $R_h(s)$ is responsible for tracking the current component at each ω_h frequency. The block diagram representation of the PMR is shown in Fig. 2.6(a).

For high values of K_{ih}, its effect on the stability can be neglected (YEPES et al., 2011). This value can be tuned to achieve the best compromise between selective filtering and dynamic response. On the other hand, K_p has a strong effect on the fast transient response through bandwidth regulation, impacting on the selective filtering. For high K_p values, the switching harmonics interfere in the current control dynamic. For this reason, it is important to ensure that the open-loop crossover frequency is lower than a decade below the switching frequency. Therefore, the maximum acceptable K_p is given by (YEPES et al., 2011):

$$K_P = \frac{R_f}{(1 - \rho^{-1})\sqrt{2}} \sqrt{2 + 2\rho^{-2} - (1 + \sqrt{5})\rho^{-1}}, \tag{2.16}$$

where $\rho = e^{\frac{R_f T_s}{L_f}}$, T_s is the sampling period. The Bode diagram of the open-loop with PMR controller is shown in Fig. 2.6(b). Note the high gains imposed by the resonant controllers.

For discretization of the PMR controller, the Tustin method with pre-warping is recommended for $R_h(s)$. This technique avoids the shift of the resonant frequencies in the z domain. Thus, $R_h(z)$ is given by (YEPES et al., 2010):

$$R_h(z) = \frac{sin(\omega_h T_s)}{2\omega_h} \frac{1 - z^{-2}}{1 - 2z^{-1} cos(\omega_h Ts) + z^{-2}}. \tag{2.17}$$

It is worth emphasizing that this type of discretization requires a considerable computational effort due to the presence of trigonometric functions.

Simpler strategies may be used. However, deviations in resonances may occur depending on the sampling frequency and the resonance frequencies (YEPES et al., 2010).

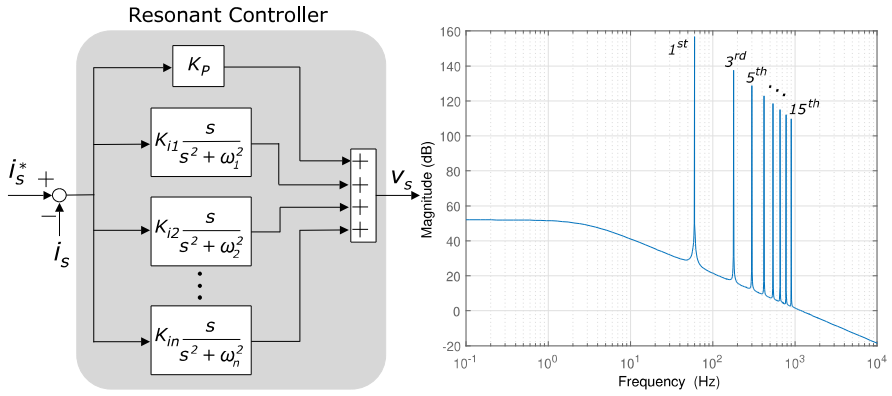

(a) (b)

Figure 2.6: (a) Block diagram representation of the proportional multi-resonant (PMR) controller. (b) Bode diagram of the open-loop with the PMR controller.

The main goal of a closed-loop control is to reject disturbances, making the control robust during variations in the plant. For this reason, the dynamic stiffness (inverse of the output impedance) is applied to the inner loop control strategy in order to verify the disturbances rejection of the system (RYAN; BRUMSICKLE; LORENZ, 1997). Considering the disturbance Δv_g in the grid voltage shown in Fig. 2.5(b), the output dynamic stiffness is found as:

$$\frac{\Delta v_g}{i_s} = -[L_f s + R_f + G_c]. \tag{2.18}$$

Therefore, the dynamic stiffness of this system is defined as the magnitude of grid voltage disturbance in each frequency that causes an unit deviation in the inverter output current. Fig. 2.7 shows the graph of the dynamic stiffness for the designed control system. Eight resonant controllers are considered, one tuned at fundamental frequency and seven tuned at the odd harmonics until the 15^{th} harmonic order. Note that, the resonant controllers insert high dynamic stiffness at each resonance frequency. Note that, the L filter effect provides high dynamic stiffness for higher frequencies.

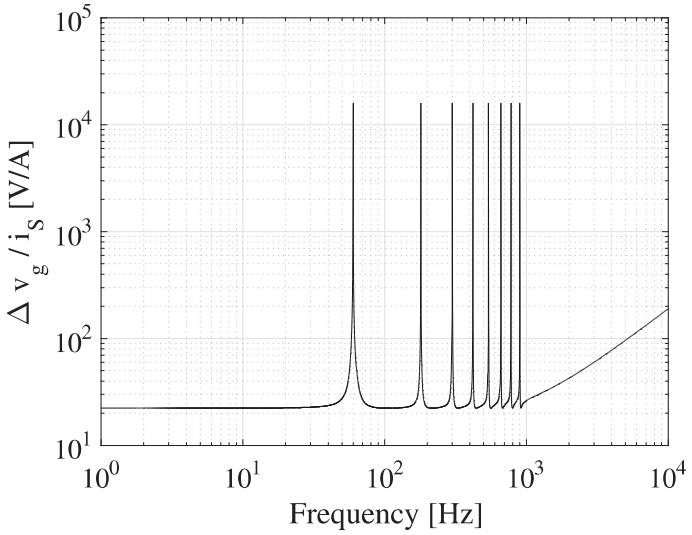

Figure 2.7: Dynamic stiffness of the inverter inner loop control ($\frac{\Delta v_g}{i_s}$).

2.4.2 Outer Loop Control: DC-Link Voltage Control

The outer loop is responsible for controlling the DC-link voltage. The method based on v_{dc}^2 control is employed (YAZDANI; IRAVANI, 2010).

The stored energy W in the DC-link capacitor can be expressed as:

$$W = \frac{1}{2} C_{dc} v_{dc}^2, \tag{2.19}$$

where C_{dc} is the capacitance of the DC-link capacitor. The capacitor's instantaneous power (P_C) is equal to the time derivative of the stored energy, as given by:

$$P_c(t) = \frac{dW}{dt} = \frac{1}{2} C_{dc} \frac{dy(t)}{dt}, \tag{2.20}$$

where $y(t) = v_{dc}^2$. Thus, Eq.(2.19) can be replaced in Eq. (2.20) and expressed in the frequency domain by:

$$P_c(s) = P_{pv}(s) - P^*(s) = \frac{1}{2} C_{dc} s Y(s). \tag{2.21}$$

where P_{pv} is the generated PV power and P^* is the PV inverter reference

power to be injected in the PCC. Isolating $Y(s)$ in Eq. (2.21), the following relation is obtained:

$$Y(s) = 2\frac{P_{pv}(s) - P^*(s)}{C_{dc}s}. \tag{2.22}$$

The closed-loop block diagram is shown in Fig. 2.8. Note that, the P_{pv} is calculated and added to the control to reduce the controller efforts. In such conditions, considering that the inner loop is fast enough and the PI transfer function $PI = K_{p_{sv}} + K_{i_{sv}}/s$, the closed-loop transfer function can be represented as:

$$\frac{Y(s)}{Y^*(s)} = \frac{K_{p_{sv}}s + K_{i_{sv}}}{\frac{1}{2}C_{dc}s^2 + K_{p_{sv}}s + K_{i_{sv}}}. \tag{2.23}$$

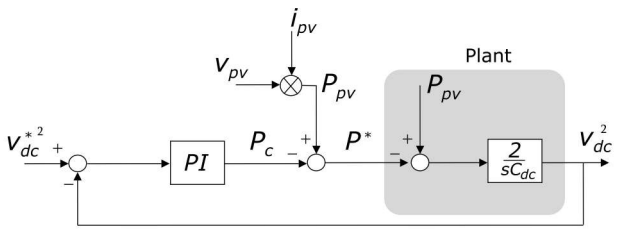

Figure 2.8: Model of the DC-link control through v_{dc}^2 based method.

Therefore, the poles are allocated in the frequencies $f_{1_{sv}}$ and $f_{2_{sv}}$, in which the first one is limited to one tenth below the bandwidth of the inner loop and the second frequency limited to one tenth below the $f_{1_{sv}}$. Therefore, applying Vieta's formulas in the denominator of Eq. (2.23), the PI gains can described by:

$$\begin{cases} K_{p_{sv}} = \pi C_{dc}(f_{1_{sv}} + f_{2_{sv}}), \\ \\ K_{i_{sv}} = 2\pi^2 C_{dc} f_{1_{sv}} f_{2_{sv}}. \end{cases} \tag{2.24}$$

2.5 DC/AC Stage Control Strategy

Until now, the inner and outer-loops modeling were presented. In this section, the presented models are combined to perform the DC/AC stage control strategy, including ancillary services such as reactive power injection and harmonic current compensation. The inverter control strategy is composed of an outer loop, designed to control the DC-link voltage and the reactive power injection to the PCC. The inner loop is designed to control the inverter current. This control strategy is shown in Fig. 2.9.

It is used the second order generalized integrator (SOGI) structure to obtain the $\alpha\beta$ components of the grid voltage at the fundamental frequency, equivalent signals to the stationary reference frame (CIOBOTARU; TEODORESCU; BLAABJERG, 2006). This structure is important in distorted grid voltage conditions. With the active power (P^*) provided by the dc-link voltage control loop and the reactive power reference (Q_F^*), the currents i_α^* and i_β^* can be found using PQ-theory given by (YANG, 2014):

$$i_\alpha^* = \frac{2}{v_\alpha^2 + v_\beta^2}(v_\alpha P^* + v_\beta Q_F^*) \tag{2.25}$$

where v_α and v_β are the grid voltage at fundamental frequency in the stationary reference frame calculated by the second order generalized integrator (SOGI) structure (CIOBOTARU; TEODORESCU; BLAABJERG, 2006). The steady state error (ΔQ) between the reactive power set-point (Q^*) and the reactive power injected by the PV inverter is added to the control.

The reactive power set-point can be provided to perform some ancillary service related to reactive power. For example, if the power factor correction is performed, the load reactive power is measured and added to the control as Q^*.

The harmonic current $\tilde{i}_L$ is detected in the load current (i_{Load}) and it is added to the inverter control loop for harmonic current compensation. This current and the fundamental current component (i_α^*), calculated by the outer-loop, are processed by the inverter current limitation techniques in order to verify if the harmonic current compensation can be partial or total. It is worth to highlight that $\tilde{i}_L$ inserts several frequency components in the inverter current reference $i_{s\alpha}^*$, which hinders the use of the PI controller. Thus,

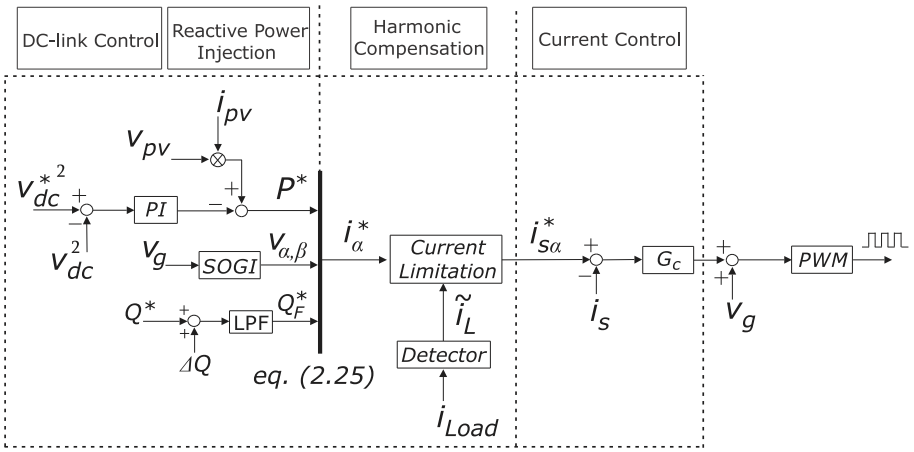

Figure 2.9: DC/AC stage control strategy for single-phase photovoltaic inverter with harmonic current compensation and reactive power injection capabilities.

the inverter current control is performed by proportional multi-resonant controllers (PMR) adjusted in each harmonic frequency to be compensated.

In the next chapters, it will be proposed two techniques to limit the peak value of the inverter current in order to perform partial harmonic current compensation and, next, an harmonic current detection method for selective harmonic current compensation.

Chapter 3

Selective Harmonic Current Compensation Strategy

In this chapter, a method for selective harmonic current compensation is presented. The method is based on SOGI-PLL structure to detect some harmonic current components. This method allows to compensate the harmonics selectively and to adaptively tune the resonant controllers. In addition, a complete analysis of the SOGI-PLL structure is developed in this chapter.

Many issues need to be addressed in order to use photovoltaic inverter to compensate harmonic currents. The first one is the harmonic current detection method. The detection methods used in harmonic compensation can be categorized in the time and frequency-domain methods.

Different strategies have been proposed in the time domain. In Paredes et al. (2011) and Bonaldo, Paredes and Pomilio (2016) is used the conservative power theory for current decomposition in three orthogonal components, the active, reactive and residual current component. In Akagi, Kanazawa and Nabae (1984) and Watanabe, Akagi and Aredes (2008) it is used the instantaneous power theory to separate the current in average and oscillating components. Tummuru, Mishra and Srinivas (2014) use the instantaneous symmetrical components theory for extracting the current references.

The methods cited above are widely used but they detect all the harmonic components. As previously mentioned, total harmonic compensation may not be possible for photovoltaic systems at certain periods of the day and may overload the PV inverter. For this reason, there are strategies for

selective detection of harmonics. Rodriguez et al. (2011) propose a multiresonant frequency locked loop (FLL) based on SOGI to detect the harmonic components selectively. However, only one FLL is used in order to detect the fundamental frequency component, and for detecting the other harmonics this frequency is multiplied by the respective harmonic order. Also, this information is used to tune the SOGIs structures. Therefore, this structure is not adaptive, the harmonic components to be compensated are pre-defined.

There are detection methods in frequency domain such as discrete Fourier transform (DFT) (MCGRATH; HOLMES; GALLOWAY, 2005), (GONZALEZ; GARCIA-RETEGUI; BENEDETTI, 2007) and the fast Fourier transform (ASIMINOAEI; BLAABJERG; HANSEN, 2005). The disadvantage of these strategies is that the settling times are limited to the windowing time period, generally one fundamental period. In addition, the requirement for this strategy is that the harmonic should be constant during the windowing interval (ASIMINOAEI; BLAABJERG; HANSEN, 2005).

Most of these methods mentioned above were developed and adapted to be used in active filters, which are designed to perform only the grid harmonic compensation. For this reason, this work introduces a harmonic detector algorithm able to detect the harmonic current selectively and adaptively applied in PV systems, where there are several functions being performed in some moments there is no current margin to compensate all the harmonic current components. Therefore, the goal of this strategy is compensate as much harmonic components as possible, respecting the physical limits of the PV inverter.

This work proposes a harmonic current detection method based on second order generalized integrator (SOGI) associated with the syncronous reference frame-phase-locked loop (SRF-PLL) (XAVIER et al., 2017). Generally, this structure is used as grid synchronization method for power converters. The SRF-PLL structure for single-phase systems is shown in Fig. 3.1 (KAURA; BLASKO, 1997), (TEODORESCU; LISERRE; RODRIGUEZ, 2011). A quadrature signal generator provides a stationary reference frame and then the $\alpha\beta \rightarrow dq$ transformation is used to convert the reference frame of the input voltage from $\alpha\beta$ to dq. The angle of the input signal is estimated by this closed-loop structure that cancels the quadrature axis voltage and the direct axis component aligns with the voltage space vector.

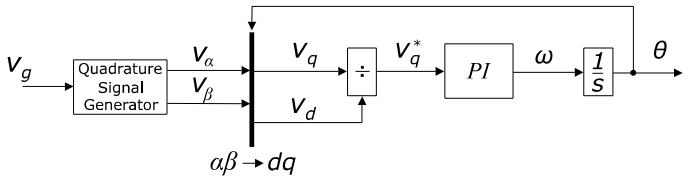

Figure 3.1: SRF-PLL structure (KAURA; BLASKO, 1997).

The quadrature axis component of the grid voltage normalized by the amplitude can be written as:

$$v'_q = sin(\theta_o - \theta), \tag{3.1}$$

where $\theta_o = \omega_o t + \phi_o$. ω_o and ϕ_o are the fundamental frequency and phase-angle. When the PLL tracks the signal, $\theta = \theta_o$ and v_q becomes zero.

Note a nonlinear dynamics of the PLL. Considering small signal in order to linearize this system, it is reasonable to consider that $sin(\gamma) \approx \gamma$ for $\gamma \approx 0$. Therefore, considering the PI control transfer function $PI = K_{p,pll} + K_{i,pll}/s$, the closed-loop transfer function which relates the input angle (θ_o) and the tracking angle (θ) can be represented as:

$$\frac{\theta}{\theta_o} = \frac{G(s)}{s + G(s)} = \frac{K_{p,pll}s + K_{i,pll}}{s^2 + K_{p,pll}s + K_{i,pll}}, \tag{3.2}$$

where it is a standard second-order transfer function. For this reason, it is defined $K_{p,pll} = 2\zeta\omega_n$ and $K_{i,pll} = \omega_n^2$, where ζ is the damping factor and $\omega_n = 2\pi f_n$ is the SRF-PLL natural frequency. In order to obtain an acceptable dynamic performance of the phase angle detection process, $\zeta = 1/\sqrt{2}$ is recommended in the literature and ω_n is adjusted in accordance with the desired controller bandwidth (GOLESTAN; GUERRERO, 2015).

A quadrature signal generator is the adaptive filter SOGI (CIOBOTARU; TEODORESCU; BLAABJERG, 2006). This structure is recommended under distorted conditions in the input signal, once it is able to generate two quadrature signals filtered at the frequency detected by the PLL, as shown in Fig. 3.2. The SOGI transfer functions are represented as:

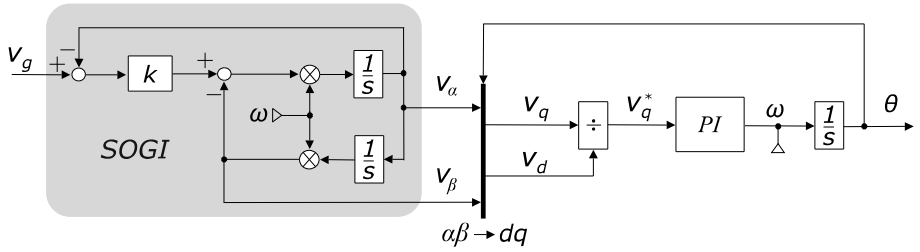

Figure 3.2: Complete structure of the SOGI-PLL.

$$H_\alpha = \frac{v_\alpha}{v_g} = \frac{k\omega s}{s^2 + k\omega s + \omega^2}, \tag{3.3}$$

$$H_\beta = \frac{v_\beta}{v_g} = \frac{k\omega^2}{s^2 + k\omega s + \omega^2}, \tag{3.4}$$

where k is the SOGI gain. Eqs. (3.3) and (3.4) suggest that the SOGI structure is both bandpass and low-pass filter, respectively. An important characteristic of the SOGI-PLL structure is that the bandwidth and cutoff frequency only depends on the gain k. Fig. 3.3 shows the Bode diagram of the SOGI transfer functions for three different values of k gain. Note that, for low values of k, the bandwidth and the cut-off frequency of the SOGI are lower.

The harmonic current detection method proposed in this work is based on two or more cascaded SOGI-PLL, as shown in Fig. 3.4. The resonance frequency of the SOGI-based adaptive filter (SOGI-based AF) is provided by the SRF-PLL frequency feedback (CIOBOTARU; TEODORESCU; BLAABJERG, 2006). In addition, the harmonic current detection structure consists of two stages.

The first detector stage is responsible for detecting the parameters of the load current fundamental component, such as its frequency ($\omega_f = 2\pi 60$ rad/s) and amplitude. The input current of this stage is composed of the fundamental component and several signals of different harmonic orders (h), represented by the following equation.

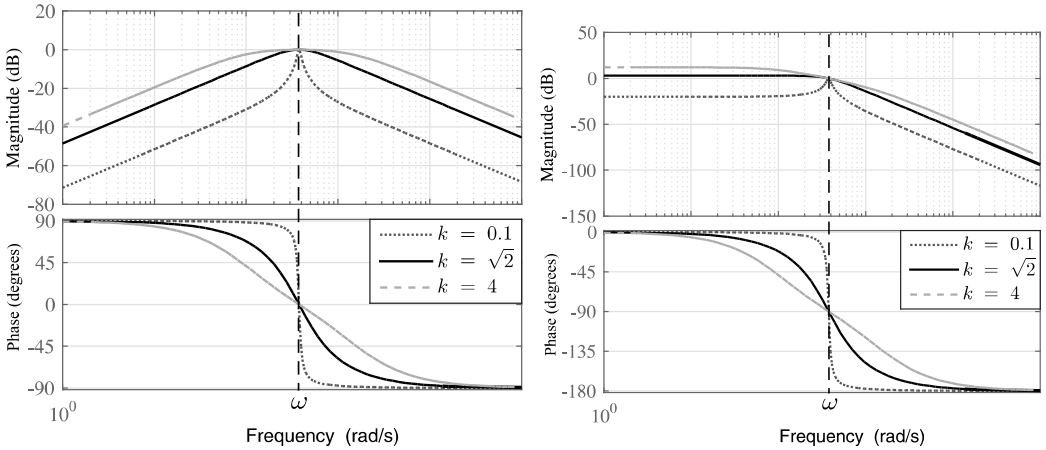

Figure 3.3: Bode diagrams of the SOGI for tree values of the gain k(a) H_α transfer function. (b) H_β transfer function.

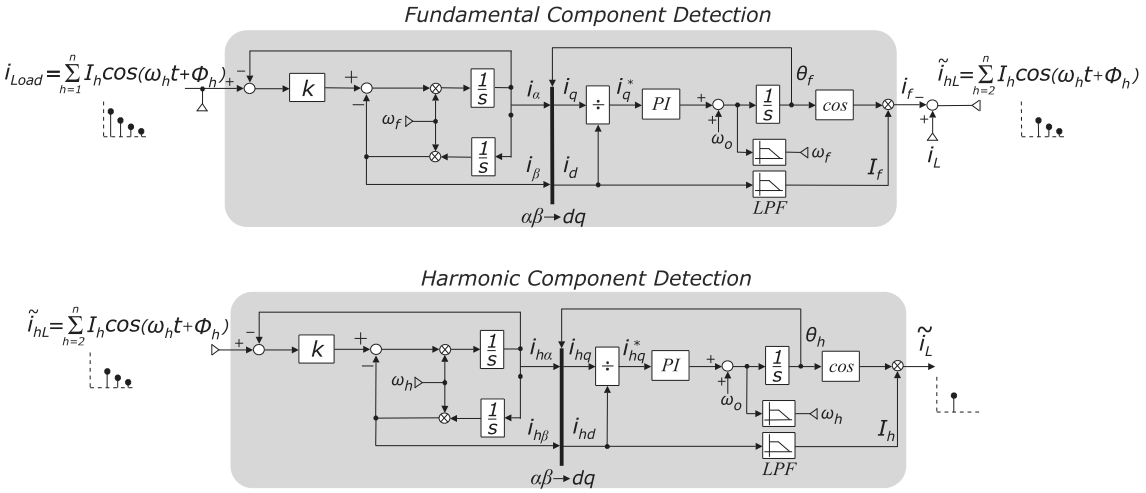

Figure 3.4: Current harmonic detection method based on two cascaded SOGI-PLL.

$$i_{Load} = \sum_{h=1}^{n} I_h cos(\omega_h t + \phi_h), \tag{3.5}$$

where the capital latter (I_h) represents amplitude of each harmonic component of the input current. ω_h and ϕ_h is angular frequency and phase angle of the signals. Generally, in the electrical power system the odd-numbered

harmonics of the fundamental frequency are more common. However, in Eq. (3.5) the harmonic pairs are also considered, making the analysis more generic.

In the SRF-PLL, the convention adopted in this work is to design the dq reference frame angular position in order to make i_q to zero. Therefore, the amplitude of the current fundamental component I_f is equal to i_d filtered by a low-pass filter (LPF). Therefore, the fundamental current component i_f is detected as:

$$i_f = I_f cos(\theta_f), \tag{3.6}$$

where θ_f is the fundamental component phase angle detected by the SRF-PLL. All input current harmonic content ($\tilde{i}_{hL}$) is determined by the difference between the input current i_L and the detected fundamental frequency i_f.

The second stage is similar to the previous one. However, it is responsible for detecting the predominant harmonic current component. The harmonic frequency ω_h and amplitude I_h of the signal are detected in this stage. The harmonic component $\tilde{i}_L$ is determined as:

$$\tilde{i}_L = I_h cos(\theta_h), \tag{3.7}$$

where θ_h is the detected harmonic component phase angle. Furthermore, the second stage is also responsible for the adaptive characteristic of the proposed current control, i.e., the detected harmonic frequency is used to adjust the PMR controller.

The structure presented above can be extended to detect any number of harmonic current components present in the load current, as shown in Fig. 3.5. In this structure, n SOGI-PLLs can be connected in series.

In this work, the strategy of negative feedback is included in the harmonic detector based on SOGI-PLL. This concept consists of subtracting the detected harmonic components from the input signals of the previous stages. For example, in the first stage, where the current fundamental component is detected, all harmonic currents detected by the following stages are removed from the input current i_L. Thereby, in steady state, a cleaner signal is provided for each detector stage, which reduces the effort detection of each

stage. It is worth emphasizing that each stage provides the tuning frequency for the proportional multi-resonant controller, making an adaptive control.

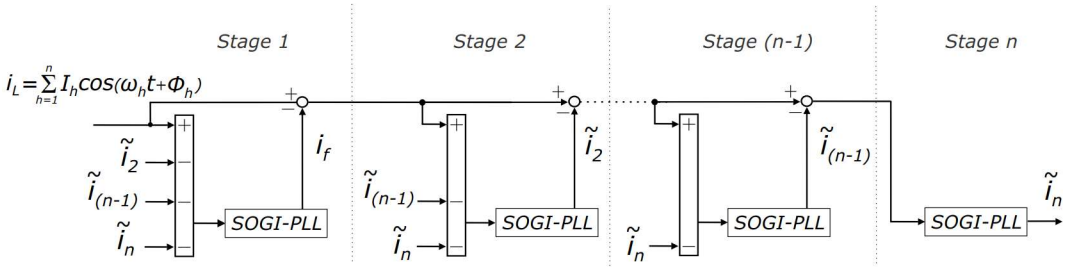

Figure 3.5: Multi-stage harmonic detector.

In the next section, a detailed analysis is performed in order to stress the proposed methodology. Among the analysis, it is highlighted the SOGI-PLL tuning process, which should ensure an admissible settling time with a flexible bandwidth to track the harmonic current component. Other important point is the effect of the cut-off frequency of the low-pass filters (LPFs), which needs to avoid unwanted oscillations in the detected amplitude and frequency.

3.1 Harmonic Detector Analysis

3.1.1 SOGI Gain Effect on the Harmonic Detection

For the proposed analysis, a input current i_L with frequency ω_h and amplitude I_h is considered, as given by:

$$i_L = I_h cos(\omega_h t). \tag{3.8}$$

The SRF-PLL feedback frequency is assumed to ideally track down the frequency, i.e., the detected frequency is ω_h. As mentioned previously, the SOGI-based AF transfer functions are expressed in Eq. (3.3) and Eq. (3.4). the signal attenuation of the SOGI increases with gain k, but with different shapes for $H_\alpha(s)$ and $H_\beta(s)$. This fact can influence the harmonic signal detection. Applying Laplace transform in Eq. (3.8), replacing it in Eqs.

(3.3) and (3.4) and applying inverse Laplace transform, the time responses of the $i_{L\alpha}$ and $i_{L\beta}$ can be obtained:

$$i_{L\alpha}(t) = I_h cos(\omega_h t) - I_h e^{(-\frac{\omega_h k t}{2})} \left[cosh(A\omega_h t) - \frac{k sin(A\omega_h t)}{2A} \right], \tag{3.9}$$

$$i_{L\beta}(t) = I_h sin(\omega_h t) + \frac{I_h e^{(-\frac{\omega_h k t}{2})} sin(A\omega_h t)}{A}. \tag{3.10}$$

where $A = \sqrt{1 - \frac{k^2}{4}}$. The first terms of the $i_{L\alpha}$ and $i_{L\beta}$ equations represent the steady state and the second terms are the dynamic transient. Note two quadrature components in steady state at the frequency ω_h. This is the ideal case, in which the SOGI can suppress any other frequency in the input signal. However, it does not happen ideally in practice. In fact, the SOGI gain k determines the filtering attenuation of the signal at frequency ω_h.

To verify the influence of the SOGI gain on the signal filtering, the PLL is disregarded and an input current (i_L) containing a 3rd harmonic order of amplitude 1 A and 5th harmonic order component with amplitude equal to 3 A is considered. The SOGI is tuned to filter the fifth harmonic. Fig. 3.6 shows the spectra of the $i_{L\alpha}$ current for four different values of the gain k. Note that the influence of the 3rd harmonic on the i_α current decreases with the gain value k. This is expected due to the reduction of the SOGI bandwidth and cutoff frequency as already illustrated in the Fig. 3.3. This fact is ignored in applications where the filtered signal has much larger amplitude than the rejected signals, such as in the grid synchronization applications. On the other hand, this work approaches a SOGI-PLL analysis for operation when the signal amplitude detected by the SOGI-PLL is similar when compared with the rejected signal amplitude. In this operating region, unwanted oscillations in the detected signal are more sensitive to the SOGI-PLL bandwidth adjustment and the low-pass filter cutoff frequency.

Analyzing Fig. 3.6, it seems obvious to choose the gain k in order to completely suppress the unwanted harmonic frequencies. In this case it seems attractive to choose $k = 0.1$, but this value represents a narrow SOGI bandwidth. This fact can reduce adaptability of the strategy to detect the predominant harmonic in a signal.

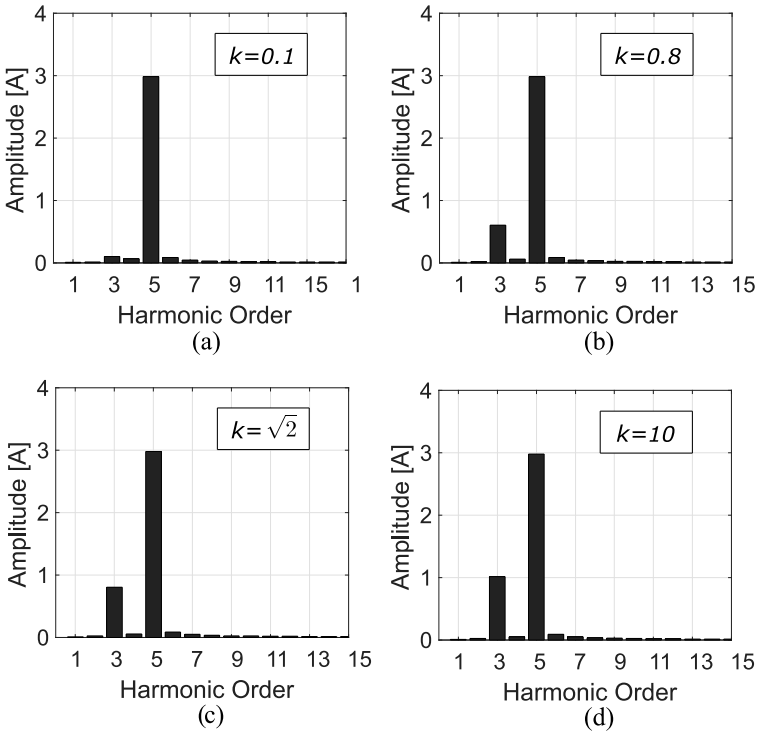

Figure 3.6: Spectra of the $i_{L\alpha}$ current for four different values of the gain k.(a) $k = 0.1$.(b) $k = 0.8$.(c) $k = \sqrt{2}$.(d) $k = 10$

In fact, the detector has a zone that limits its adaptation and can be explained by two factors. The first one is the SOGI bandwidth limitation defined by the gain k. The second one is the capability of SRF-PLL to follow the predominant harmonic component. The analysis of both phenomena are presented in this chapter.

3.1.2 SOGI Detection Threshold

To evaluate the adaptability threshold in terms of the SOGI bandwidth, an input current composed of a 3rd and 5th harmonic component is considered again. In addition, the complete SOGI-PLL structure is considered. Thereby, i_L is given by:

$$i_L = I_3 cos(\omega_3 t) + I_5 cos(\omega_5 t), \tag{3.11}$$

where $\omega_3 = 2\pi 180\ rad/s$ and $\omega_5 = 2\pi 300\ rad/s$. I_3 and I_5 are the amplitudes of the 3rd and 5th harmonic current, respectively.

The initial SRF-PLL feedback frequency is considered as ω_3 and $k = \sqrt{2}$. The H_α and H_β magnitudes of the SOGI structure are illustrated in Fig. 3.7(a) and Fig. 3.7(b), respectively. When the amplitude of 5th harmonic current component becomes higher than the 3rd harmonic component ($I_5 > I_3$), the 5th harmonic content is detected as predominant harmonic if:

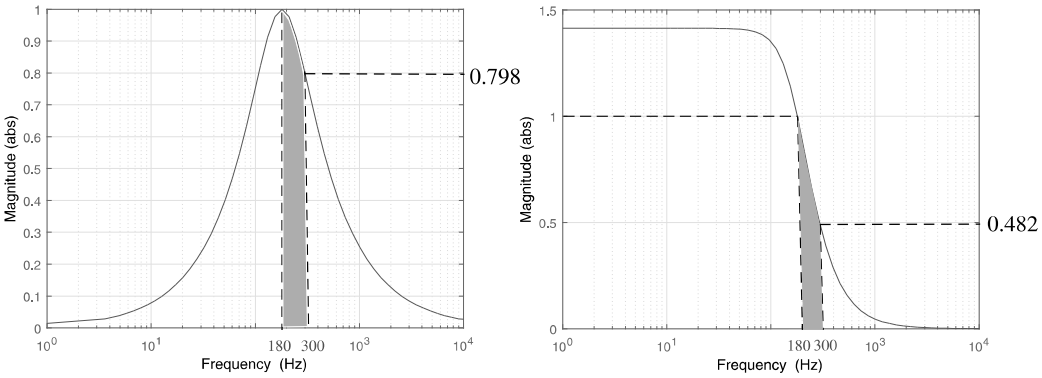

(a) (b)

Figure 3.7: Magnitude of the SOGI output signals soon after the addition of the 5^{th} harmonic to the signal.(a) H_α magnitude gain.(b) H_β magnitude gain.

$$\overbrace{I_5 \cdot 0.798 > I_3}^{R_1} \quad and \quad \overbrace{I_5 \cdot 0.482 > I_3}^{R_2}, \tag{3.12}$$

where 0.798 and 0.482 are the magnitudes at 300 Hz of the SOGI output signals, as shown in Fig. 3.7(a) and Fig. 3.7(b), respectively. Since the magnitude at 180 Hz is unitary, if I_5 does not satisfy the minimum condition R_2 in (3.12), the 5th harmonic content is not detected.

In order to check (3.12), simulations are used. Initially, considers that the SOGI-PLL is detecting the 3rd harmonic component. In 0.4 seconds, two different amplitude values of a 5^{th} harmonic component (2 A and 2.2 A) are applied in the SOGI-PLL for comparison, and the amplitude of the 3rd harmonic current signal is constant (1 A). Considering that $I_5 = 2\ A$, the expression R_2 is not satisfied. Therefore, the 5^{th} harmonic component of the

current is not detected, as shown in Fig. 3.8. For $I_5 = 2.2\ A$, the condition R_2 becomes true and the 5th harmonic content is detected, as shown in Fig. 3.8.

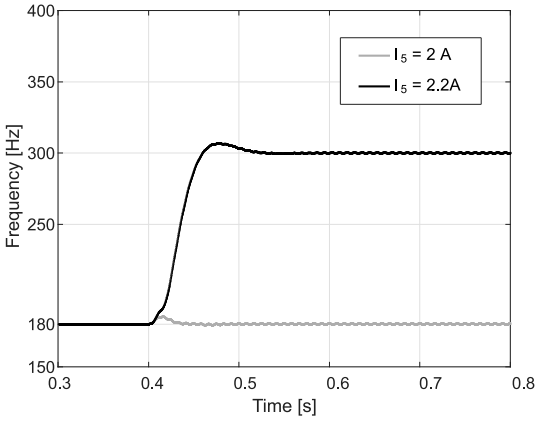

Figure 3.8: 5^{th} harmonic component detection response for two different values of I_5.

Once these analyzes have been carried out, it can be concluded that the lower the value of k the better filtering of the signal by the SOGI in steady state. However, the structure decreases its adaptability in a load variation condition. Thus, there is a tradeoff between filtering capacity and system adaptability. In this work, $k = \sqrt{2}$ is adopted and the detection error is minimized through the tuning of the LPF in the amplitude and frequency detection and the PLL natural frequency design.

3.1.3 LPF Effect on the Harmonic Detection

In the proposed harmonic detector method, the LPF has an important influence in the output characteristic, mainly when the harmonic detector input i_L has two or more harmonic components. Therefore, unwanted harmonic orders must be avoided in the amplitude and frequency detection process. In this work, the second order Butterworth low-pass filters with cut-off frequencies f_{cf} (for frequency filtering) and f_{ca} (for amplitude filtering) are used. The input current is the same used in the SOGI gain analysis.

Fig. 3.9(a) and Fig. 3.9(b) shows the influence of three f_{cf} and f_{ca} values (5 Hz, 10 Hz and 30 Hz) on the frequency and amplitude detection

of the 5th harmonic component in 0.4 seconds, respectively. In steady state conditions, the frequency ripple is 1% for $f_{cf} = 30\ Hz$, as depicted in Fig. 3.9(a), whereas the amplitude ripple for $f_{ca} = 30\ Hz$ is 4%, as shown in Fig. 3.9(b). For $f_{cf} = 30\ Hz$, besides the direct component, there is a high oscillation of 2nd harmonic in the detected amplitude I_5, as shown in Fig. 3.9(c). Therefore, unwanted 3rd and 7th harmonic components arises in the output current $\tilde{i}_L$ by the product between the 2nd harmonic oscillation and the detected phase angle of the 5th harmonic content, which can be observed in Fig. 3.9(d). In order to reduce the unwanted frequencies in the detected predominant harmonic and a fast detection response for this work $f_{ca} = 10\ Hz$ and $f_{cf} = 10\ Hz$ are adopted.

3.1.4 SRF-PLL Natural Frequency Impact on the Harmonic Detection

The PLL natural frequency f_n is adjusted in accordance with the controller bandwidth. For this reason, some values of the f_n are tested in order to verify the influence of this parameter in the harmonic current detection response.

The frequency and amplitude detection of the 5th harmonic component for some f_n values are shown in Fig. 3.10(a) and Fig. 3.10(b), respectively. It can be observed that for $f_n = 10\ Hz$, the amplitude and frequency of the 5th harmonic has not been detected. For $f_n = 100\ Hz$, an offset is observed in the detected amplitude due to SRF-PLL wide bandwidth. This wide bandwidth generates unwanted oscillations at the detected phase angle, and thus the dq reference frame angular position is affected. The acceptable relationship between settling time, unwanted oscillations suppressions and lower steady-state error is found for $f_n = 50\ Hz$.

3.1.5 SRF-PLL Detection Threshold

In fact, if the input signal of SRF-PLL is composed of two harmonics with similar amplitudes, the SRF-PLL may also limit the detector adaptability and not track the predominant harmonic in the input current signal.

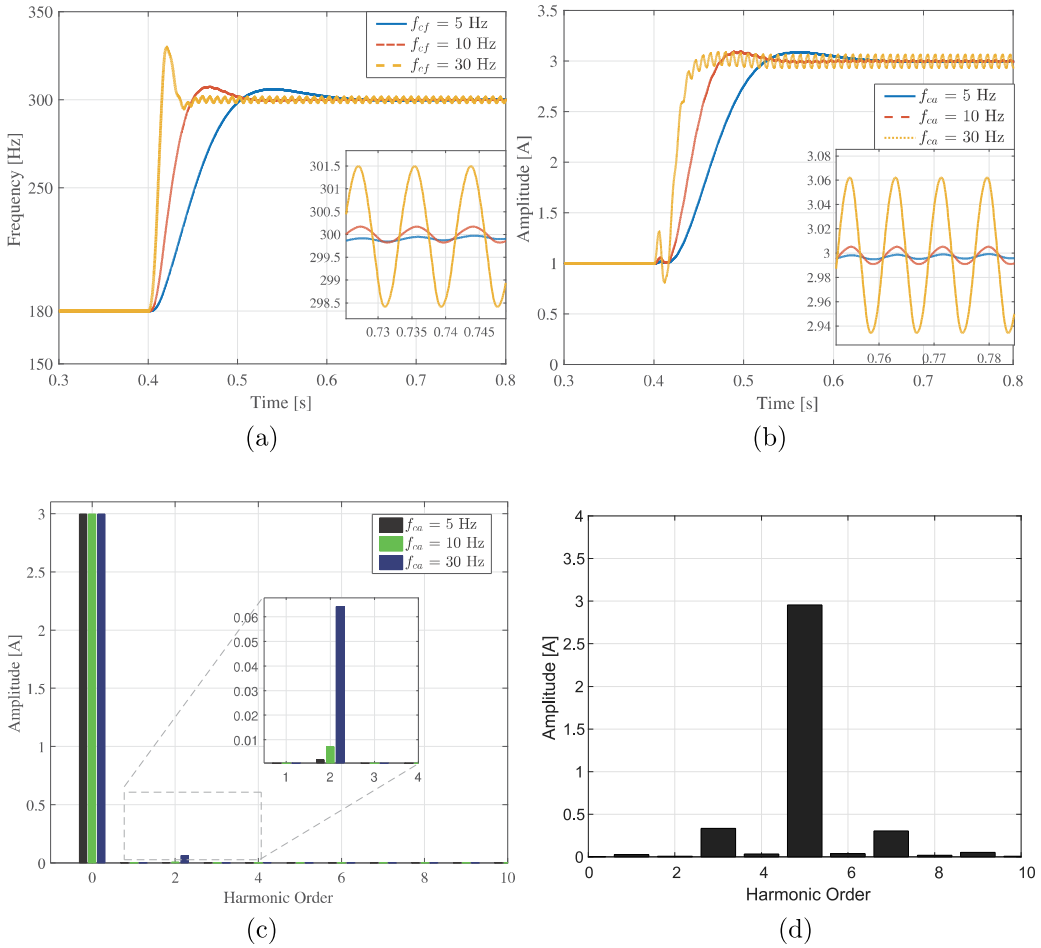

Figure 3.9: Detected frequency and amplitude for three different values for both cut-off frequencies (f_{cf} and f_{ca}) of the LPFs, considering $k = \sqrt{2}$.(a) Detected frequency for three f_{cf} values.(b) Detected amplitude for three f_{ca}, keeping $f_{cf} = 10\ Hz$.(c) Detected amplitude spectrum for three f_{ca} values, keeping $f_{cf} = 10\ Hz$. (d) Detected $\tilde{i}_L$ current spectrum, parameters: $f_{ca} = 30\ Hz$, $f_{cf} = 10\ Hz$ and $k = \sqrt{2}$

In this condition, this work defines the PLL *detection threshold*, which consists in the minimum amplitude difference between two harmonic components which implies in the transition of the detection between the two harmonic components. In order to understand the SRF-PLL detection threshold, firstly it is necessary to understand its dynamic behavior during frequency changes (single harmonic approach).

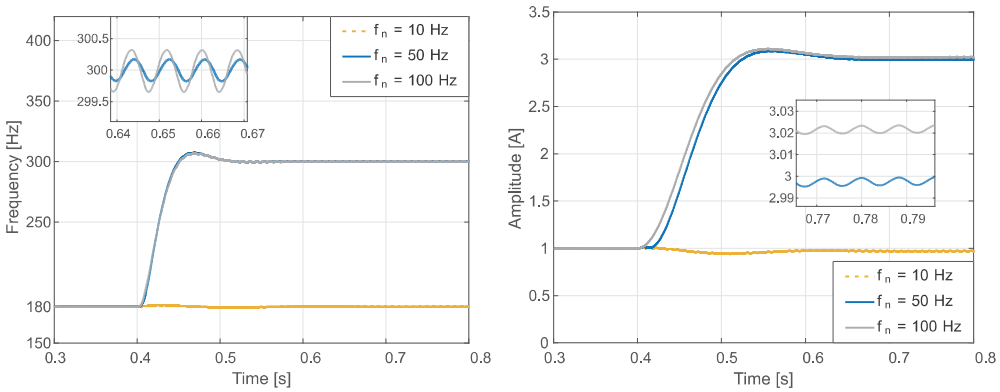

Figure 3.10: Detected frequency and amplitude for some values of SRF-PLL natural frequency f_n. Parameters: $k = \sqrt{2}$, $f_{ca} = 5\ Hz$ and $f_{cf} = 10\ Hz$.(a) Detected frequency.(b) Detected amplitude.

The SRF-PLL is a nonlinear system. The transfer function presented in Eq. (3.2) considers a locked state. However, for large frequency variation (change of harmonic content), this approach is not valid. The study of PLL's modeling in unlocked state is related in some texts in literature (BEST, 2003), (GARDNER, 2005). Using a similar methodology in Best (2003), the SRF-PLL dynamics can be modeled by the following nonlinear differential equation:

$$\ddot{\theta}_e + \dot{\theta}_e K_{p,pll} sin\theta_e + K_{p,pll} cos\theta_e + K_{i,pll} sin\theta_e = \ddot{\theta}_{in}, \tag{3.13}$$

where $\theta_e = \theta_h - \theta_{in}$ is the phase error.

The solution of this differential equation is not a trivial task. Specialized texts evaluate the performance during unlock state using some key parameters obtained from some approximations and simulations analysis (BEST, 2003), (GARDNER, 2005), (TEODORESCU; LISERRE; RODRIGUEZ, 2011).

For two or more harmonic components, the determination of these parameters is more complex. Some texts in literature approaches this problem considering the main component much larger than other harmonics. In this case, these harmonic components can be modelled as a noise signal (GARDNER, 2005). However, this approach is not valid for the proposed harmonic detector. Numerical solutions can be used in order to solve this problem, for specific values of ξ and ω_n. Thus, it is possible to estimate the SRF-PLL

detection threshold.

To illustrate this process, initially, it is used a 1 pu of 3^{rd} harmonic signal in the SRF-PLL input. When it reaches the steady-state, a 5^{th} harmonic component is added in the SRF-PLL input signal. The amplitude value of 5^{th} harmonic component is slowly increased, in order to determine the SRF-PLL detection threshold.

The study case results are presented in Fig. 3.11. It can be observed that the detection threshold reduces significantly for large ξ and ω_n. However, large ξ results in poor dynamic behaviour as mentioned in Teodorescu, Liserre and Rodriguez (2011). Furthermore, large ω_n increases the amplitude offset and the estimated frequency ripple, as presented previously. For the chosen parameters, the detection threshold is close to 1.4 pu. This value is smaller than the threshold imposed by the SOGI bandwidth, as seen before. Therefore, for the adjustment considered in this work, the SRF-PLL structure does not reduce the adaptability of the harmonic detector.

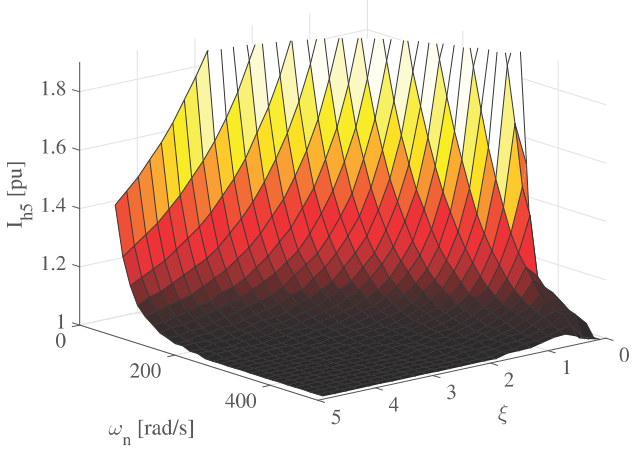

Figure 3.11: SRF-PLL detection threshold in function of ξ and ω_n considering a transition from 3rd to 5th harmonic order.

3.2 Simulation Results

A case study in simulation environment is used in order to validate the harmonic current detector based on the SOGI-PLL structure for selective harmonic current compensation. In this case study, the solar irradiance is held constant in 300 W/m^2.

The physical and control parameters of the boost converter used in this work are shown in Table 3.1. The parameters of the PV inverter are shown in Table 3.2.

Table 3.1: Parameters of the boost converter.

Physical Parameters	**Value**
Inductor (L_b/R_b)	0.8 mH / 0.01 mΩ
Capacitor (C_{pv})	0.5 mF
Switching frequency (f_s)	12 kHz
Inner-Loop Control Parameters	**Value**
Proportional gain (K_{pi})	0.0155
Integral gain (K_{ii})	0.1933
Outer-Loop Control Parameters	**Value**
Proportional gain (K_{pv})	-0.7540
Integral gain (K_{iv})	-132.27

Table 3.2: Parameters of the PV inverter.

LCL Parameters	**Value**
Inverter side inductor (L_i/R_i)	1.5 mH / 0.03 mΩ
Grid side inductor (L_g/R_g)	1.5 mH / 0.03 mΩ
Capacitor (C_f)	0.1 μ F
Damping resistor (R_d)	4 Ω
Physical Inverter Parameters	**Value**
Inverter Rated power (S_m)	3 kVA
Inverter rated current (I_m^*)	19.3 A
DC-link Capacitor (C_{dc})	3 mF
Switching frequency (f_s)	12 kHz
Inner-Loop Control Parameters	**Value**
Proportional gain (K_p)	22.24
Resonant gains (K_{ih})	2000
Outer-Loop Control Parameters	**Value**
Proportional gain (K_p)	0.2
Integral gain (K_i)	2.37

The two loads shown in Fig. 3.12 are switched at the PCC at 1.4 seconds. The maximum demand PCC current at the fundamental frequency used for the TDD calculation is 19.3 A.

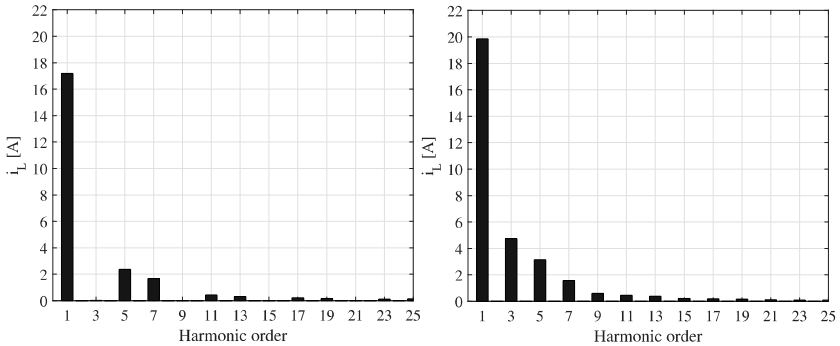

Figure 3.12: Current spectra of two nonlinear loads used in the simulation case study. (a) Load 1. (b) Load 2.

The harmonic current detector based on the SOGI-PLL structure, proposed in this work, is used to detect only two predominant harmonic components, in terms of amplitude, in the load current. As described previously, three stages of the detector are required, the first one responsible to detect the fundamental current component and others two responsible to detect the predominant harmonic contents. This harmonic detector tuning the PMR controller frequencies adaptively. In such conditions, three resonant controllers are used, one to control the fundamental component and others two for the harmonic current component to be compensated.

Fig. 3.13 shows the amplitudes and frequencies detection of the two predominant harmonic current of load 1 and 2. As already mentioned, the harmonic detector is based on SOGI-PLL structure and there are three stages. The first one responsible for detecting the fundamental component of the load current, as shown in Fig. 3.13(a). As can be seen in Fig. 3.13(b), the amplitude and frequency of the predominant harmonic current are detected in stage 2. Initially, the 5^{th} harmonic of the load 1 is detected and after $t = 1.4$ seconds the 3^{rd} is detected. Fig. 3.13(c) shows the detection of the second predominant harmonic current by the stage 3. First, the 7^{th} harmonic current is detected and after $t = 1.4$ seconds the 5^{th} harmonic current of the

load 2 is detected. The three resonant controllers used in this case study are adaptively tuned by the three detected frequencies in stage 1, 2 and 3.

The spectra of the two predominant harmonic currents detected from load 1 and load 2 are shown in Fig. 3.14(a) and (b), respectively. The 5^{th} and 7^{th} harmonic component are predominant in terms of amplitude in load 1. In load 2, the 3^{rd} and 5^{th} harmonic component are predominant.

The improvement of the grid current quality with selective harmonic current compensation can be seen through the current spectra, as shown in Fig. 3.15. This figure shows the spectra of the load, inverter and grid current in steady state before and after the load change in 1.4 seconds. Before 1.4 seconds, the 5^{rd} and 7^{th} harmonic, presented in the current of the load 1, are totally provided by the inverter, as shown in Fig. 3.15(a). In this case, the grid current TDD is 6.90%. It is worth highlighting that if there were no harmonic compensation, the grid current TDD would be equal to load current, in this case 20.36%.

After 1.4 seconds, the 3^{rd} and 5^{th} harmonic, presented in the current of the load 2, are totally provided by the inverter, as shown in Fig. 3.15(b). In this case, the grid current TDD is improved from 52.72% to 14.35%.

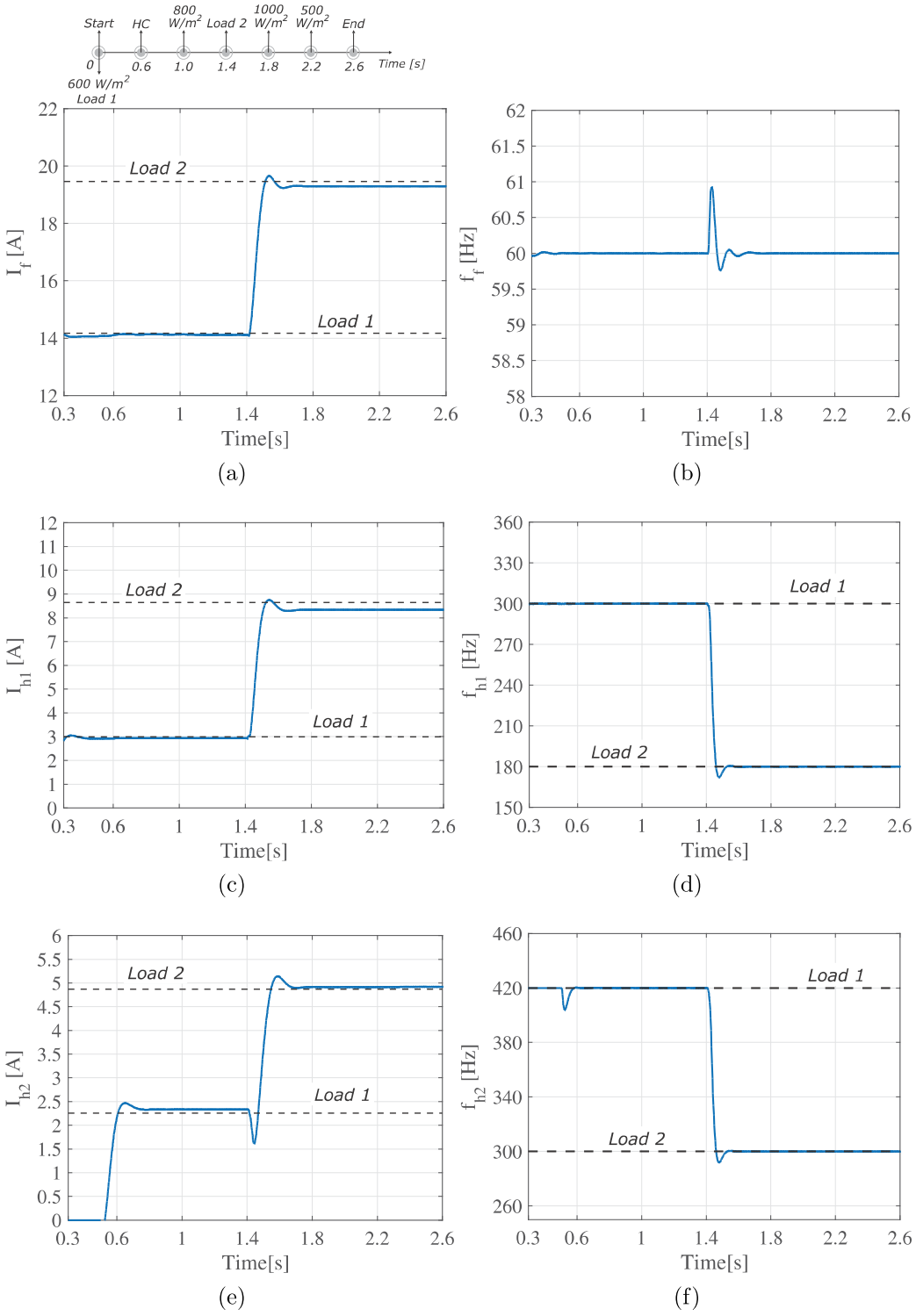

Figure 3.13: Detected harmonic current components of the load current using the SOGI-PLL structure. (a) Fundamental current peak detected in stage 1. (b) Detected fundamental frequency.(c) Predominant harmonic current peak detected in stage 2. (d) Detected frequency of the predominant harmonic. (e) Current peak of the second predominant harmonic current detected in stage 3. (f) Detected frequency of the second predominant harmonic.

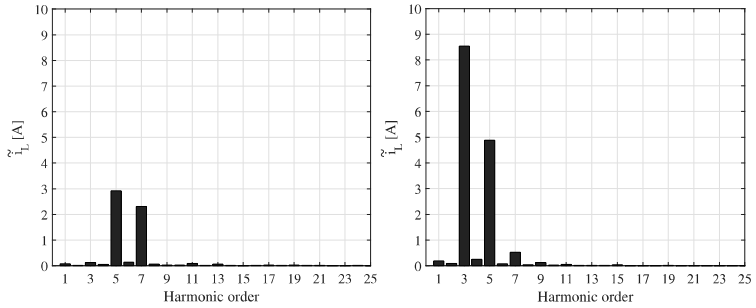

Figure 3.14: Detected current spectrum. (a) Load 1. (b) Load 2

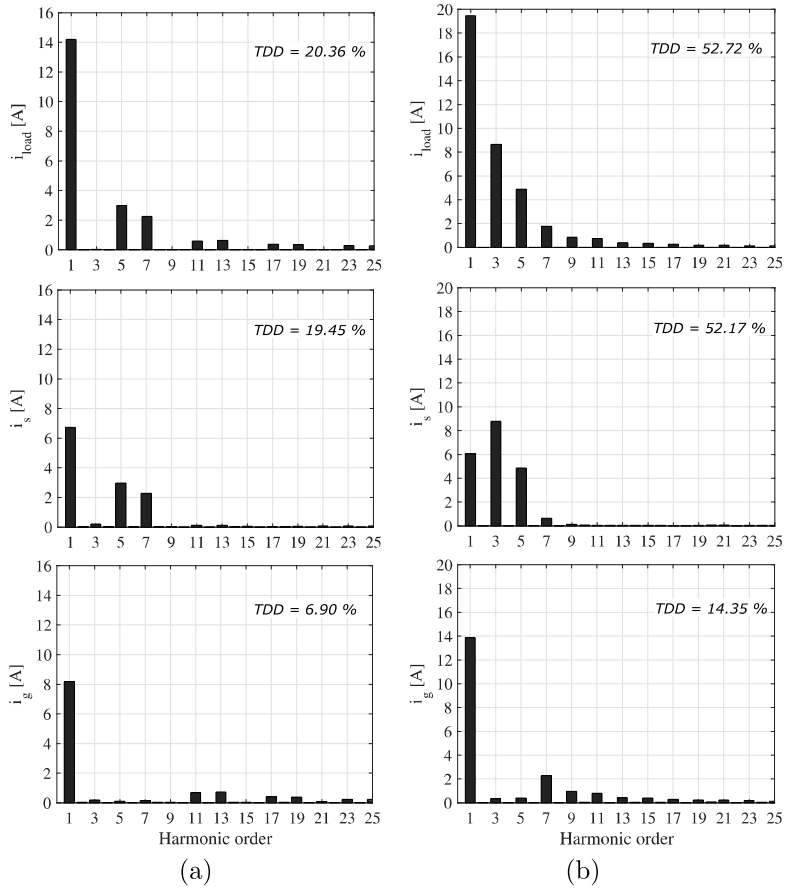

Figure 3.15: Spectra of the load (i_{Load}), inverter (i_s) and grid (i_g) current in steady state before and after the load change in 1.4 seconds . (a) Before 1.4 seconds. (b) After 1.4 seconds

3.3 Experimental Results

A case study in experimental environment is made in order to validate the harmonic current detector based on the SOGI-PLL structure for selective harmonic current compensation. The developed prototype is based on the simplified PV system shown in Fig. 2.5(a). The DC/DC stage and DC-link voltage control are not considered. The focus of the strategies for partial harmonic current compensation are entirely applied in the inverter current control loop. For this reason, only the inverter inner loop control is considered in the experimental test. Therefore, in order to ignore the DC side control, The DC-link voltage is ensured using an external power supply. Thus, the control strategy shown in Fig. 2.9 is implemented without the outer loop.

An overview of the designed prototype can be seen in Fig. 3.16. A Semikron power module is used to implement the single-phase full bridge inverter (SEMIKRON, 2006). This power module presents two full bridge converters but only one is used. Some parameters of this power module are shown in Table 3.3. The parameters of the case study are presented in Table 3.4.

Table 3.3: power module parameters.

Parameters	**Value**
Maximum switching frequency	15 kHz
DC-link maximum voltage	750 V
DC-link capacitance	3.06 mF

Table 3.4: Experimental System Parameters.

Parameters	**Value**
Grid voltage (v_g)	127 V / 60Hz
DC-link voltage (v_{dc})	370 V
Filter inductance (L_f)	4 mH
Switching frequency (f_s)	9 kHz
PMR Controller Gains	**Value**
Proportional gain (K_p)	20 A/V
Resonant gains (K_{ih})	2000 A/V

The control is performed through the kit eZdsp F28335 150 MHz from Spectrum Digital. This device presents 12 PWM channels, 16 analog-to-

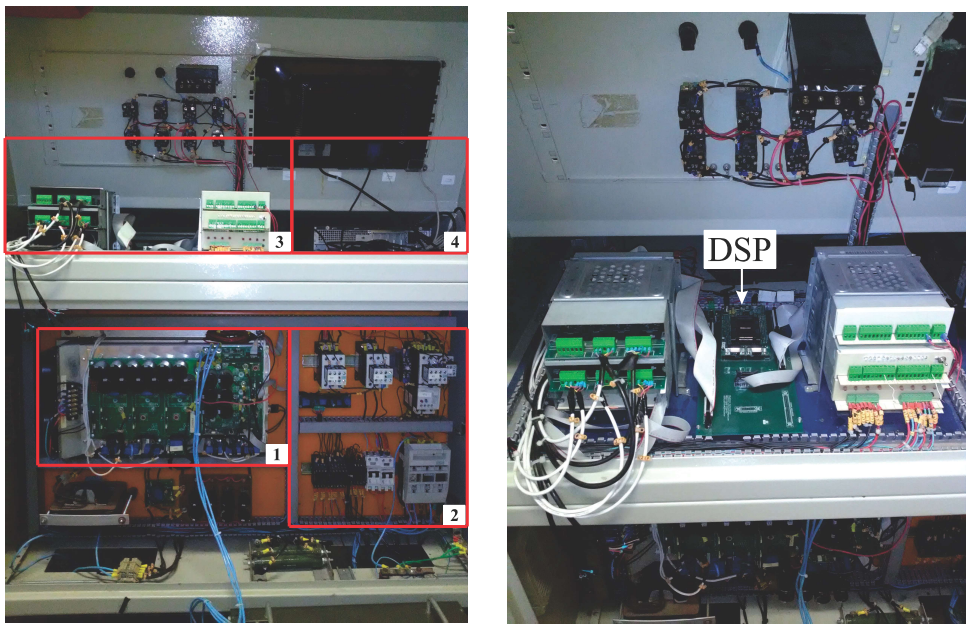

(a) (b)

Figure 3.16: Setup of the designed prototype. (a) Setup overview: 1- Power module. 2- Control circuit. 3- Conditioning and control boards. 4- Microcomputer. (b) Conditioning and control boards.

digital converter of 12 bit and 512 KB of FLASH memory. The signal conditioning system can be seen in Fig. 3.16.

A nonlinear load based on diode rectifier was designed with variable harmonic current content. The schematic of this load is shown in Fig. 3.17. This load is started in three-phase mode, thus contactors 2 and 1 are closed. A resistor R_{PC} is used to pre-charge the capacitor bank. A timer sets a time for this pre-charge by closing the contactor 3 in order to bypass the resistor R_{PC}. Once this is done, the load current can be varied between three-phase and two-phase through the contactor 2. Thus, a single-phase inverter connected in any phase P, E or T experiences a change in the harmonic content of the current. The setup overview and inside view of this nonlinear load are shown in Fig. 3.18. The current spectrum of load 1 is shown in Fig. 3.19(a). In load 1, the 5^{th} and 7^{th} harmonic components are predominant in term of amplitude. Fig. 3.19(b) shows the current spectrum of load 2, which the 3^{rd} and 5^{th} harmonic are predominant. Initially, load 1 is connected to

the PCC.

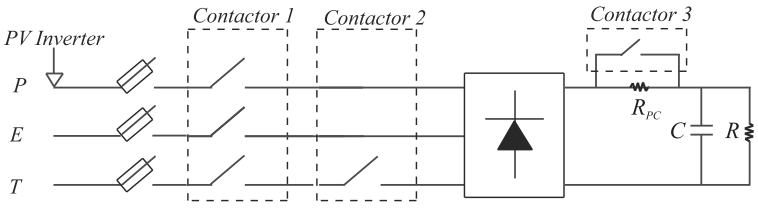

Figure 3.17: Schematic of the designed nonlinear load.

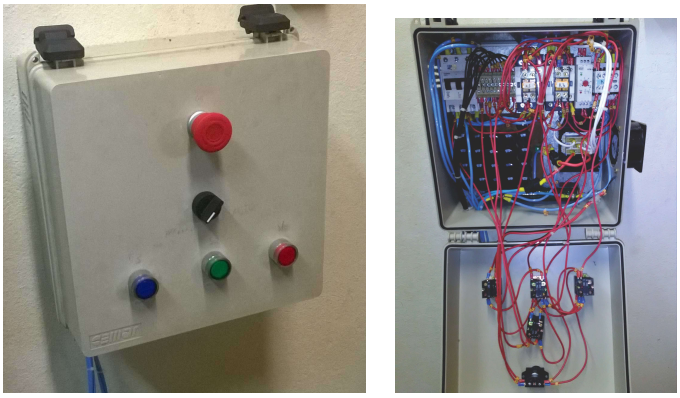

(a) (b)

Figure 3.18: Designed nonlinear load. (a) Setup overview. (b) Setup inside view.

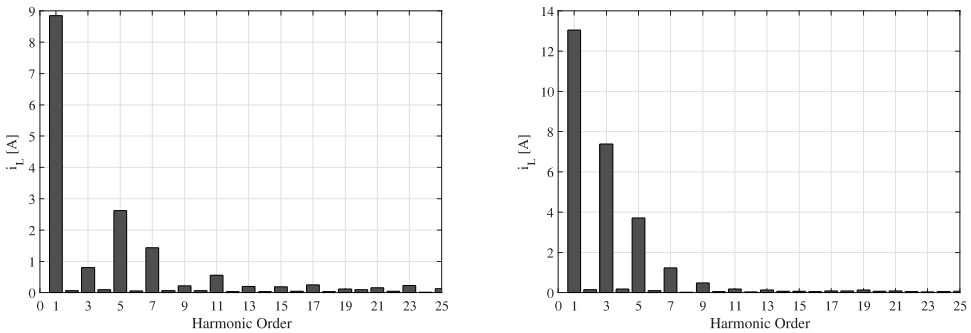

(a) (b)

Figure 3.19: Current spectra of two nonlinear loads used in this experimental case study. (a) Load 1. (b) Load 2.

The goal of the harmonic current detector based on SOGI-PLL is to track the two predominant harmonic current components of the two loads, in order to perform harmonic current compensation. Therefore, three stages of this detector are used. The PMR controller presents three resonant controllers in which their resonance frequencies are adjusted adaptively by the harmonic current detector.

In this case study, 2 A of the fundamental current is injected by the inverter, emulating the active power injection of the PV system.

The amplitude and frequency detection of the fundamental component, when load 1 is switched to load 2 at the PCC, is shown Fig. 3.20. The detector tracks 9 A of the load 1, and after 13 A of load 2, as shown in Fig. 3.20(a). The detected fundamental frequency is 60 Hz, as expected. It is important to highlight that all the detected frequencies are used to tune the PMR controller adaptively.

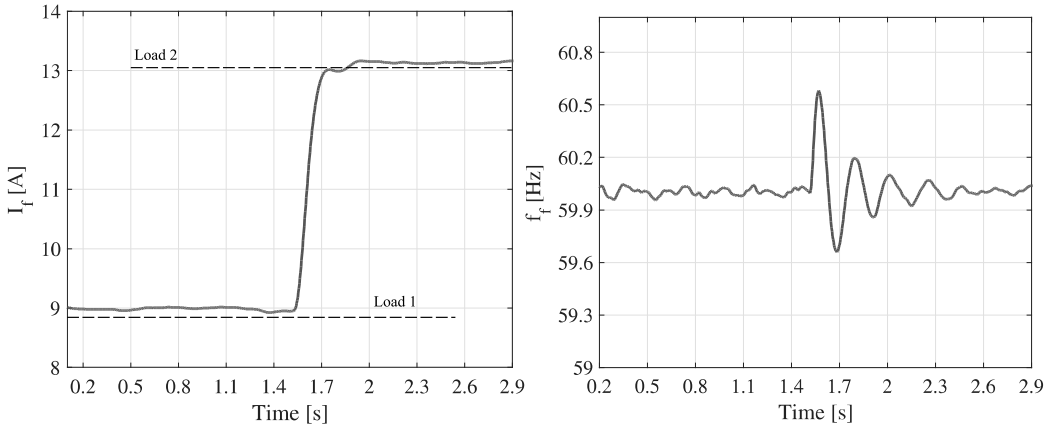

(a) (b)

Figure 3.20: Detection of the fundamental component performed by the first stage of the harmonic current detector. (a) Amplitude. (b) Frequency.

The stage 2 of the detector is responsible for detecting the predominant harmonic current component. The dynamic behavior of the detected amplitude and frequency in this stage during load variation is shown in Fig. 3.21. When load 1 is connected, 5^{th} harmonic of 2.6 A is detected. After wards, load 2 is connected and the predominant harmonic becomes the 3^{rd} harmonic.

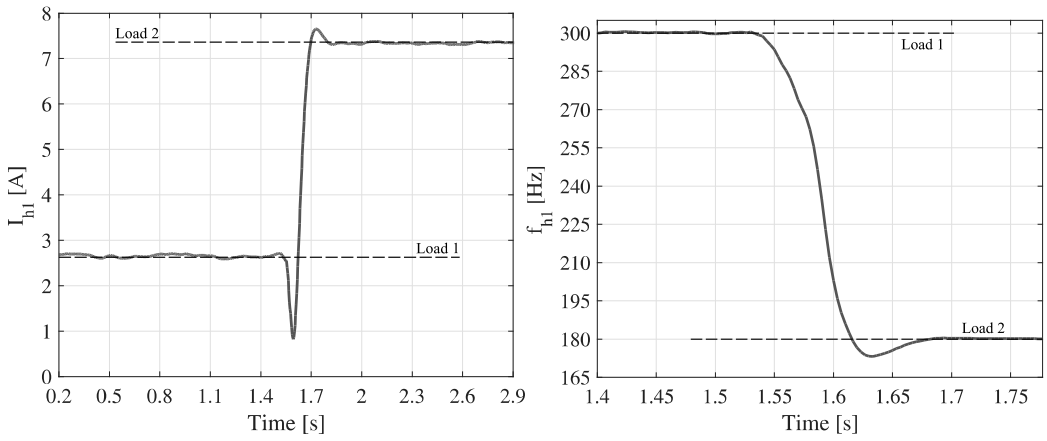

Figure 3.21: Detection of the predominant harmonic component performed by the second stage of the harmonic current detector. (a) Amplitude. (b) Frequency.

The stage 3 of the detector is responsible to detect the second predominant harmonic current component. The dynamic behavior of the detected amplitude and frequency in this stage, during load variation, is shown in Fig. 3.22. When load 1 is connected, 5^{th} harmonic of 2.6 A is detected. After, load 2 is connected and the predominant harmonic becomes the 3^{rd} harmonic. This last stage is the most overloaded because all remaining harmonic contents enter in this stage. For this reason, it is normal to observe some errors in the amplitude detection.

The load, inverter and grid current waveforms and their respective spectra during harmonic current compensation of the two predominant harmonic components of the load 1 are shown in Fig. 3.23. Before the harmonic compensation, the grid current was equal to the load current and its TDD was 25.78 %. With harmonic compensation of the 5^{th} and 7^{th} harmonic, the grid current TDD is 7.62 %. The injected fundamental current is too small, emulating low solar irradiance condition. The peak value of the inverter current is 7 A. Thereby, the inverter provides an interesting grid power quality improvement without great efforts.

The load, inverter and grid current waveforms and their respective spectra during harmonic current compensation of the two predominant harmonic

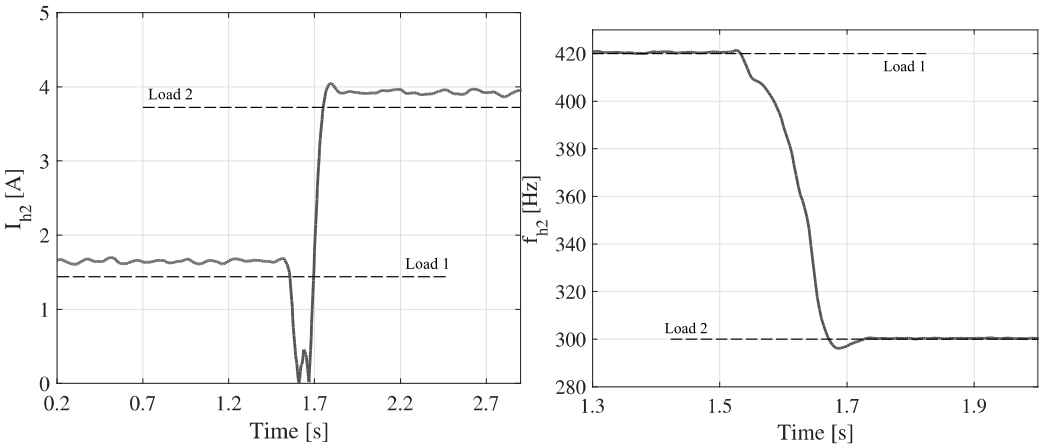

Figure 3.22: Detection of the second predominant harmonic component performed by the third stage of the harmonic current detector. (a) Amplitude. (b) Frequency.

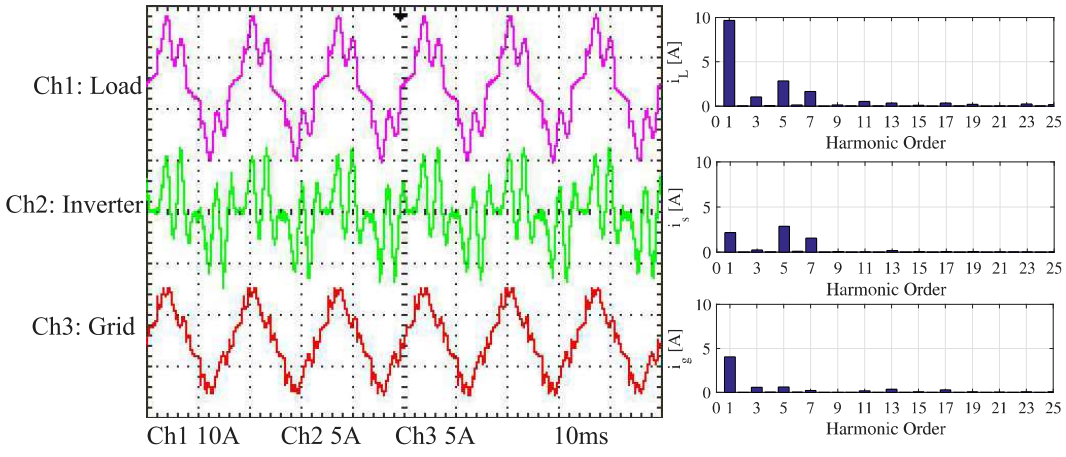

Figure 3.23: Current waveforms and spectra during harmonic compensation of the load 1.

component of load 2 are shown in Fig. 3.24. Before the harmonic compensation, the grid current was equal to the load current and its TDD was 66.25 %. With harmonic compensation of the 5^{th} and 7^{th} harmonic, the grid current TDD is 11 %. The peak value of the inverter current is 16 A.

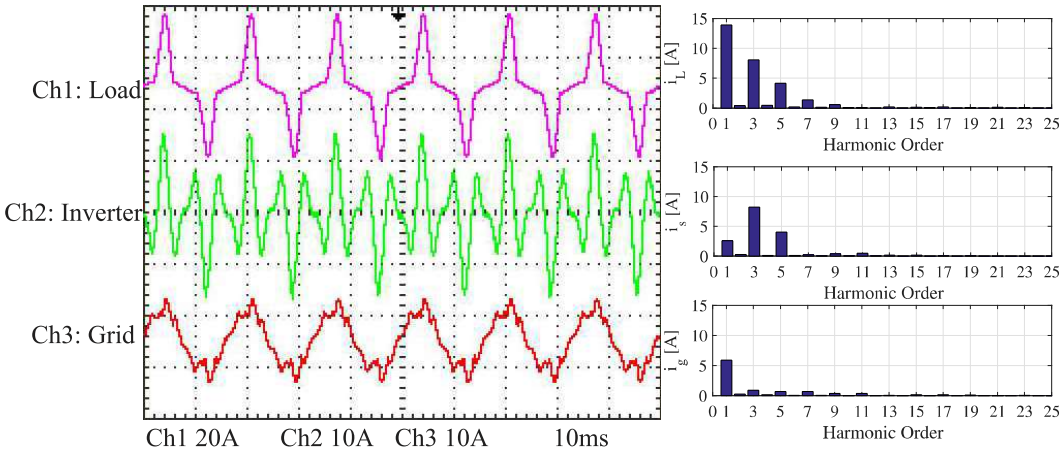

Figure 3.24: Current waveforms and current spectra during harmonic compensation of the load 2.

An experimental case study was performed to validate the methodology for selective harmonic current based on SOGI-PLL structure. Two predominant harmonic components of the load current were compensated. The adaptability of the detector could be checked during load variation.

Chapter 4

Partial Harmonic Current Compensation Strategy

To avoid inverter damages and to preserve its lifetime, the inverter rated current can not be exceeded. Thereby, techniques for PV inverter current limitation are required during ancillary services support. The critical point is when harmonic current compensation is involved. In this condition, there are multiple frequencies in the current signal and analytical expressions for inverter current limitation are complex.

Some works in the literature have been introducing techniques to limit the inverter current reference under harmonic compensation conditions. In (GAJANAYAKE et al., 2009) a current limiting algorithm is employed based on PI controller. A moving window RMS calculator is used to determine the RMS value of the current and it is compared with the maximum current limit of the inverter. The generated error signal is the input of a PI controller to reduce the harmonic current injection. However, limiting the RMS current value when there are multiple frequencies in the signal is not effective since the current peak can be much larger than the RMS value, exposing the PV inverter electronic switches to high current levels.

Therefore, this work proposes techniques to limit the peak value of the inverter current for partial harmonic current compensation. These techniques are independent of the harmonic current detection method. The first one is based on a open-loop algorithm which monitors the peak of the inverter current reference and reduces the detected harmonic current. Another technique is presented based on a closed-loop with a PI controller in order to cancel

the error between the peak value of the inverter current and its rated current. The controller output reduces the detected harmonic current in order to ensure that the inverter does not inject a peak current greater than the maximum allowed. These strategies are detailed and compared below.

4.1 Open-Loop Technique

This work proposes an inverter current limitation technique based on open-loop algorithm. This inverter current limitation scheme is presented in Fig. 4.1. The load harmonic current ($\tilde{i}_L$), the fundamental current reference (i^*_α) and the total the total inverter current reference (i^*_{st}) are inputs of the algorithm. The harmonic current limitation (HCL) algorithm determines the contribution value of the $\tilde{i}_L$ and i^*_α to the peak value of i^*_{st} and then, this algorithm calculates the factor (K_h) which determines the amount of load harmonic current that can be injected in order to ensure that the peak value of the inverter current reference ($i^*_{s\alpha}$) does not exceed the inverter rated current I^*_m. Fig. 4.2 shows the flowchart of the HCL algorithm and its step-by-step operation is described below.

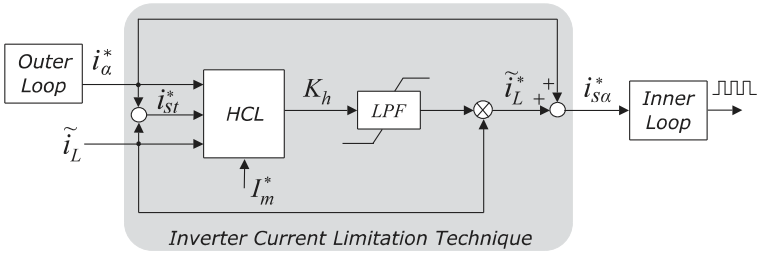

Figure 4.1: Inverter current limitation technique based on open-loop algorithm.

- The fundamental current reference (i^*_α), the load harmonic current reference ($\tilde{i}_L$) and the total inverter current reference (i^*_{st}) are HCL algorithm inputs. i^*_{st} is found by the sum between i^*_α and $\tilde{i}_L$;

- At each sampling, the value of the i^*_{st} is checked in order to obtain the peak value of this current. If the new i^*_{st} value is higher than its previous one, the M variable is updated for this new value and the

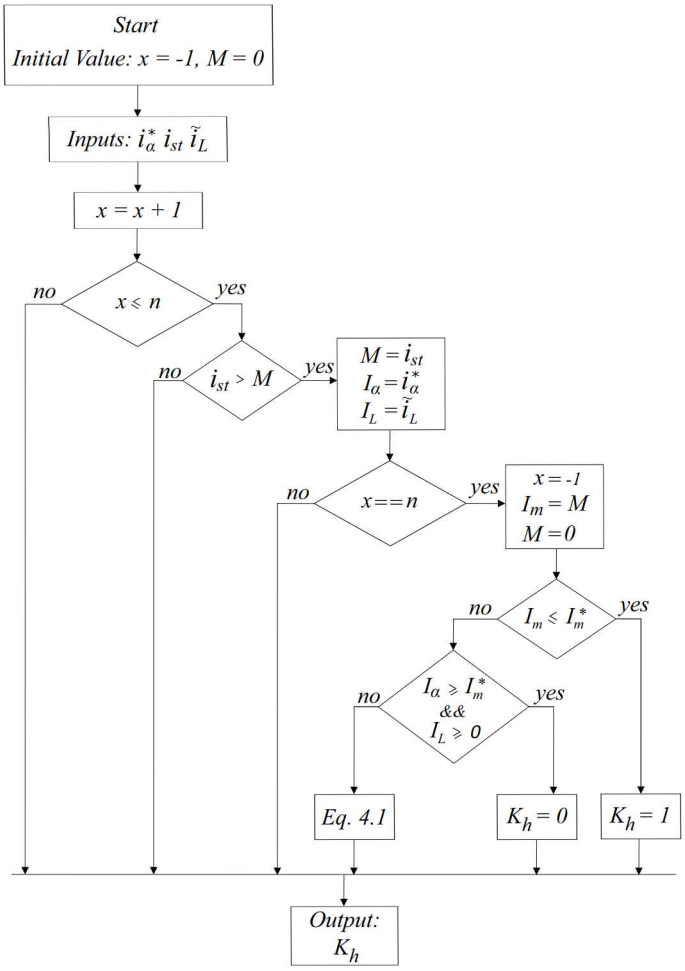

Figure 4.2: Flowchart of the harmonic current limitation (HCL) algorithm.

contributions of i_α^* and $\tilde{i}_L$ for this i_{st}^* value are stored in I_L and I_α, respectively;

- After n samples, the peak value of i_{st}^* is detected, which is referred as I_m. Furthermore, the contributions of I_L and I_α for this peak value are detected. The number of samples n is chosen in order to obtain a fundamental frequency cycle;

- The peak value (I_m) of i_{st}^* is compared to inverter rated current I_m^*. If I_m is less than I_m^*, there is current margin for total harmonic compensation, i.e., $K_h = 1$. However, if I_m is greater than I_m^*, the inverter cannot perform the total harmonic compensation;

- If I_α is greater than or equal to I_m^* and the harmonic current contribution (I_L) is positive, the harmonic current compensation is disabled, i.e., $K_h = 0$. Otherwise, the harmonic compensation will be partial and determined by proportion ratio defined as:

$$K_h = \frac{I_m^* - I_\alpha}{I_L}. \tag{4.1}$$

  This equation means that the sum of I_α and of I_L multiplied by the factor K_h must be at most equal to the inverter rated current (I_m^*);

- Finally, before the factor K_h acts on the load harmonic current ($\tilde{i}_L$), a low-pass filter (LPF) is used to suppress oscillations due to the abrupt variations in the activity of the algorithm. The filter output is limited between 0 and 1. Therefore, the harmonic current reference ($\tilde{i}_L^*$) that will be compensated can be represented as:

$$\tilde{i}_L^* = K_h \overbrace{\sum_{h=1}^{n} I_h cos(\omega_h t + \phi_h)}^{\tilde{i}_L}. \tag{4.2}$$

  This new value of the harmonic current reference is added to fundamental current component (i_α^*) and the new inverter current reference ($i_{s\alpha}^*$) is found. Note that, $i_{s\alpha}^*$ will be equal to i_{st}^* only if $K_h = 1$.

Fig. 4.3 illustrates an example of the application of this inverter current limitation technique. It is possible to see the fundamental current reference (i_α^*) provided by the inverter outer-loop control, the load harmonic current (i_L), the total inverter current reference (i_{st}^*) resulting from the sum of i_α^* and i_L, the harmonic current reference (i_L^*) resulting from the K_h factor action and the inverter current reference ($i_{s\alpha}^*$) resulting from the sum of i_α^* and i_L^* . In addition, the inverter rated current (I_m^*) is set to 19.3 A.

Fig. 4.3(a) shows the input currents of the HCL algorithm. The fundamental current contribution (I_α) to the peak value of i_{st}^* is 14.5 A. On the other hand, the harmonic current contribution (I_L) to the peak value of i_{st}^* is 12 A. Therefore, the peak value (I_m) of i_{st}^* is 26.5 A. Note that it exceeds the inverter rated current. Once the priority of the system is to inject active power, i_{st}^* peak value can only be reduced by reducing $\tilde{i}_L$ contribution. Thereby, through (4.1), it is calculated the amount of contribution $\tilde{i}_L$ can provide to the peak of i_{st}^*. Therefore, Fig 4.3(b) shows that the contribution

of i_L is reduced by the K_h factor for 40 %, which results the $\tilde{i}_L^*$ with contribution of 4.8 A. Thus, the peak value of $i_{s\alpha}^*$ is 19.3 A, which is equal to the inverter rated current.

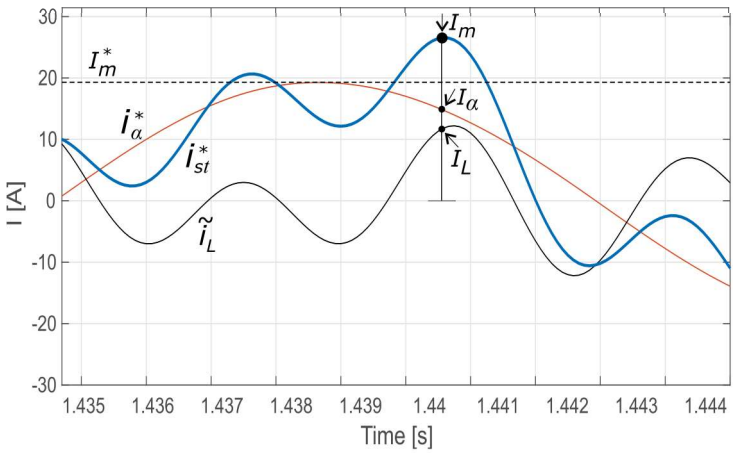

(a)

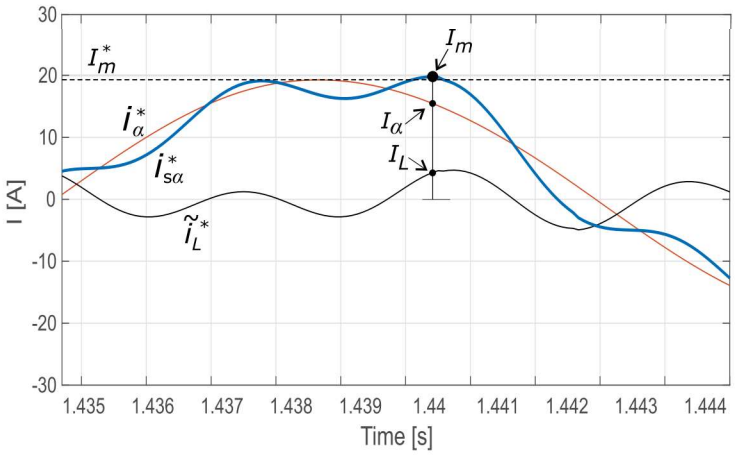

(b)

Figure 4.3: Details of waveforms of the currents during harmonic current compensation. (a) Total inverter current reference (i_{st}^*), i.e, without K_h factor action. (b) Inverter current reference ($i_{s\alpha}^*$), i.e, with K_h factor action.

4.2 Closed-Loop Technique

Another technique proposed in this work to perform partial harmonic current compensation is based on the PI controller action. Therefore, a closed-loop control is designed to calculate the K_h factor used to adjust the harmonic current reference. This closed-loop control is illustrated in Fig. 4.4.

The inverter current reference ($i^*_{s\alpha}$) is calculated by the sum between $\tilde{i}^*_L$ and the fundamental current reference i^*_α calculated by the outer loop. A current peak detector monitors the peak absolute value of this current, which is compared with the inverter rated current (I^*_m). An anti-windup PI controller, limited between 0 and 1, computes the harmonic compensation factor K_h that weights the load harmonic current ($\tilde{i}_L$), which results in the new harmonic current reference ($\tilde{i}^*_L$) in order to cancel the error between I^*_m and I_m.

Part of the HCL algorithm is used to detect the peak absolute value of $i^*_{s\alpha}$, which corresponds to $I_m$in the flowchart shown in Fig. 4.2. For this technique, the number of samples n, used in the algorithm, is chosen in order to obtain a fundamental frequency half cycle. For this reason, this algorithm inserts a delay of a fundamental half cycle in the closed-loop shown in Fig. 4.4. It is also important to highlight that the factor K_h weighs the detected harmonic component at the same frequency as that of the peak detector activity.

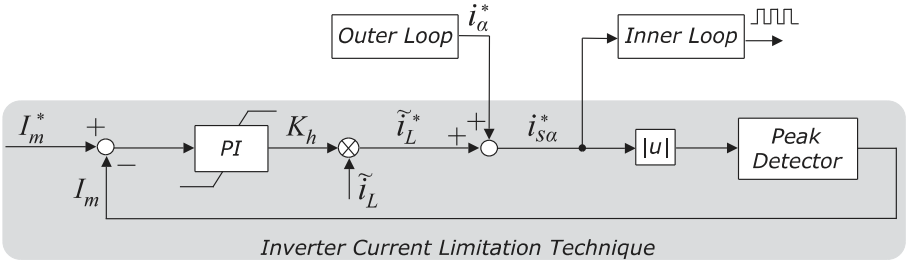

Figure 4.4: Inverter current limitation technique based on PI controller.

One important challenge of this technique is designing the PI controller gains. In fact, the PI controller design of the PI controller deserves caution to avoid instabilities. For such, it is used part of the first technique concept previously approached. The peak value (I_m) of the inverter current reference

can be determined as:

$$I_m = K_h I_L + I_\alpha, \tag{4.3}$$

It is assumed that I_L is constant and I_α is a system disturbance. These two quantities can be found by the HCL algorithm. This is a reasonable approximation due to the intermittent characteristic of the photovoltaic energy generation, i.e., variations in PV power generation are greater than a considerable load harmonic current variation during the day. Thereby, the closed-loop control modeling can be developed, as shown in Fig. 4.5.

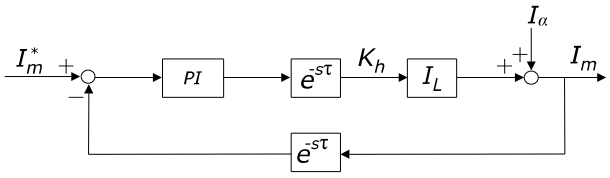

Figure 4.5: Closed-loop control modeling of the current limitation technique based on PI controller.

The terms $e^{-s\tau}$ refer to the delays accounted for the peak detection algorithm and K_h activity. These delay functions can be approximated by a rational function using the first order Padé approximation method, as described below:

$$e^{-s\tau} = \frac{1 - s\frac{\tau}{2}}{1 + s\frac{\tau}{2}}. \tag{4.4}$$

Therefore, the main goal of this closed-loop control is to reject the I_α disturbance due to variation in the PV power generation. The transfer function which relates the peak value of the inverter current reference (I_m) and the system disturbance (I_α), making the reference I_m^* equal to zero, can be expressed as:

$$E(s) = \frac{I_m(s)}{I_\alpha(s)} = \frac{1}{1 + R(s)}, \tag{4.5}$$

where $R(s)$ is given by:

$$R(s) = I_L \frac{(k_p s + k_i)(\tau s - 2)^2}{s(\tau s + 2)^2}, \tag{4.6}$$

where $K_{p,sat}$ and $K_{i,sat}$ are the PI controller gains. These gains are designed in order to achieve the better disturbance rejection performance. For this purpose, the step response analysis of the $E(s)$ transfer function is a good alternative to determine the appropriate k_p and k_i values. The peak value I_m is detected every half cycle of the fundamental frequency of 60 Hz. Then, $\tau = 1/120$ seconds. Fig. 4.6 shows the step response of the $E(s)$ transfer function for $K_{p,sat} = 0.08$, $K_{i,sat} = 5$ and $I_L = 5$ A. As observed, the closed-loop rejects the step disturbance, which makes $I_m(\infty) \approx 0$.

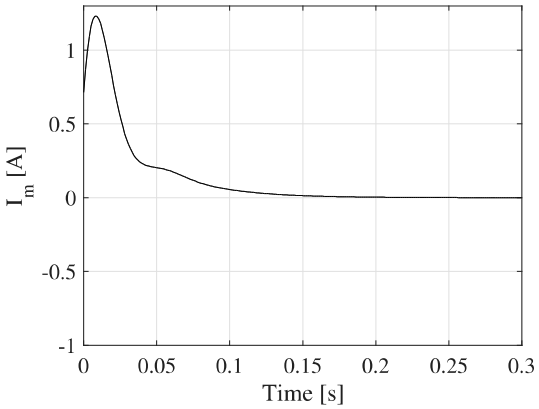

Figure 4.6: Disturbance rejection analysis through the step response of the $E(s)$ transfer function.

A comparison between these two techniques for inverter current limitation and the model of the closed-loop based method is performed in a simulation environment, considering the permissible inverter rated current (I_m^*) equal to 20 A. A variable fundamental current component is injected, whose amplitude changes from 20 A to 15 A, in steps of 1 A. In addition, a $5th$ harmonic current is injected with $I_L = 5$ A. The cut-off frequency of the low-pass filter present in the open-loop technique is 15 Hz. The computed K_h is shown in Fig. 4.7(a). As observed, the transient response of the closed-loop technique and the model present similar dynamics. The noticeable difference is due to the Padé approximation of the time delay function. The computed K_h in steady-state, depending on the injected fundamental current, is shown in Fig. 4.7 (b). It is possible to note the similarity between these techniques

in steady state.

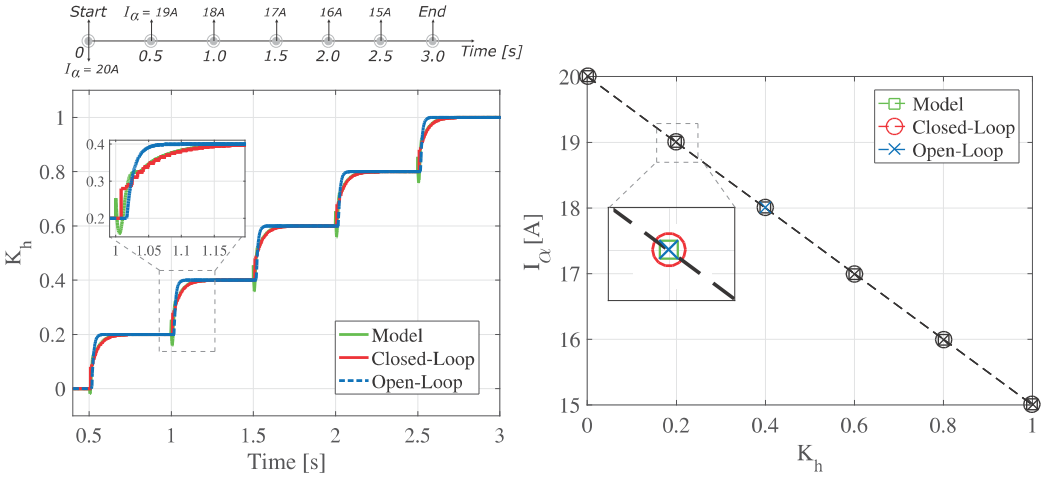

(a) (b)

Figure 4.7: K_h factor calculation comparison between the two techniques for inverter current limitation and the model of the closed-loop technique. (a) Time response of the K_h factor. (b) Steady-state response of the K_h factor in relation to the fundamental current reference injected by the inverter.

4.3 Simulation Results

The single-phase grid-connected PV system with ancillary service capability is simulated using the MATLAB® and PLECS® software in order to validate the inverter current limitation techniques for partial harmonic current compensation. In the simulation, ancillary services such as harmonic current compensation and reactive power injection are performed. The parameters of the boost converter for the DC/DC stage and the inverter are the same already presented in Tabele 3.1 and 3.2, respectively.

Two loads are switched at the PCC in order to analyze the behavior of the PV system control strategy addressed in this work. The current spectrum of the load 1 is shown in Fig. 4.8(a). Besides the fundamental component, there are odd components multiple of the fundamental frequency, except those of triple orders. Fig. 4.8(b) shows the current spectrum of load 2, with odd

harmonics, including those of triple orders. Initially, the load 1 is connected to the PCC.

Different from the case study presented in the previous chapter. All the odd harmonic frequencies of the load current (i_{Load}) until the $15th$ harmonic order are compensated in this case study . Thus, eight resonant controllers are required in the PMR controller, one to control the fundamental component and seven to control the harmonic components. For this case study, the harmonic current reference ($\tilde{i_L}$), added to the control, is equal to the current detected by the stage 1 of the detector method based on SOGI-PLL structure shown in Fig. 3.4.

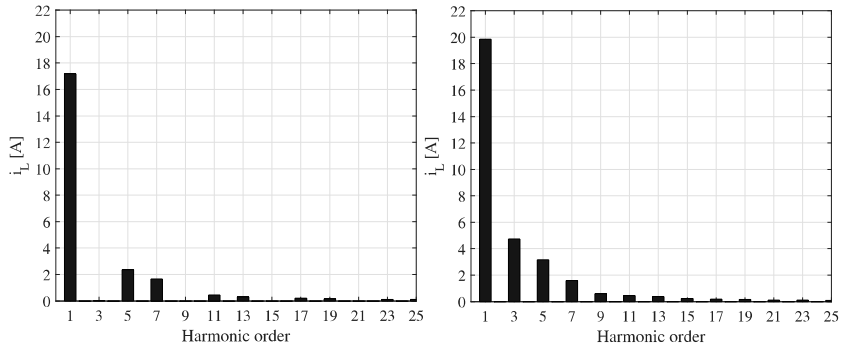

Figure 4.8: Current spectra of two nonlinear loads used in the simulation case study. (a) Load 1. (b) Load 2.

In the simulation, the solar irradiance is changed to validate the proposed techniques for inverter current limitation, under environmental change conditions. The simulation starts with load 1 connected to the PCC and irradiance of 600 W/m^2. In addition, the PV inverter injects reactive power from the beginning of the simulation, always respecting the current margin available for this service. The harmonic current compensation is enabled at 0.6 s. At $t = 1$ second, the solar irradiance changes to 750 W/m^2. The load 2 replaces the load 1 at $t = 1.4$ seconds. The solar irradiance is changed two more times, to 1000 W/m^2 and to 300 W/m^2 at $t = 1.8$ and $t = 2.2$ seconds, respectively. The maximum demand PCC current at the fundamental frequency used in the TDD calculation is 19.3 A.

The output PV array voltage (v_{pv}) is illustrated in Fig. 4.9(a), whose the

reference voltage (v_{pv}^*) is calculated by the MPPT algorithm. When the solar irradiance is 1000 W/m^2, v_{pv} corresponds to the maximum power point equal to 188 V, approximately. The boost converter inductor current is shown in Fig. 4.9(b). The DC-link voltage is controlled in 390 V, as shown in Fig. 4.9(c). The reactive power injection starts at the beginning of the simulation and the harmonic current compensation (HCC) is enabled at $t = 0.6$ seconds.

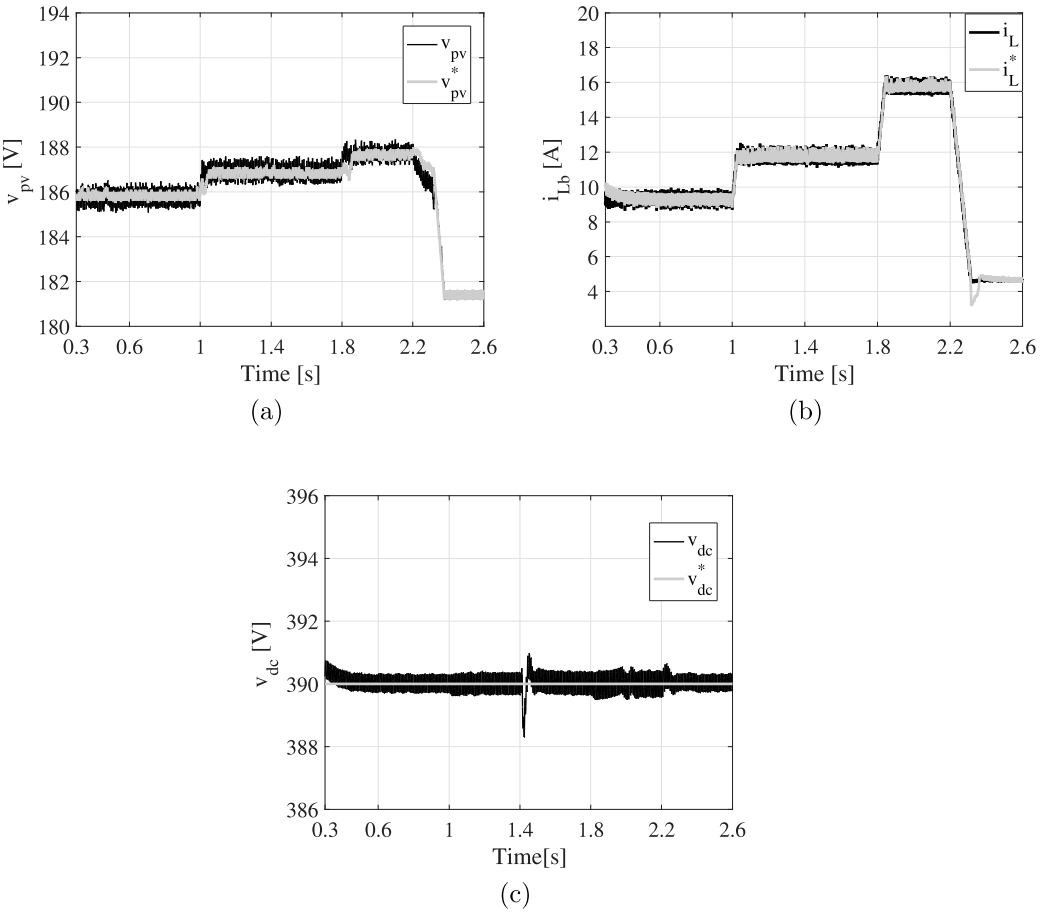

Figure 4.9: Voltage and current dynamics of the PV system DC-side. (a) Output PV array voltage (v_{pv}). (b) Inductor current of the boost converter. (c) Dc-link voltage v_{dc}.

The active (P) and reactive (Q) power dynamics are shown in Fig. 4.10. At $t = 1.8$ seconds, the PV system provides all active power to the the load, as shown in Fig. 4.10(a). At this moment, there is no inverter power margin

for reactive power injection, as shown in Fig. 4.10(b). At other times, the inverter operates below its nominal power capacity, allowing it to inject all reactive power required by the load.

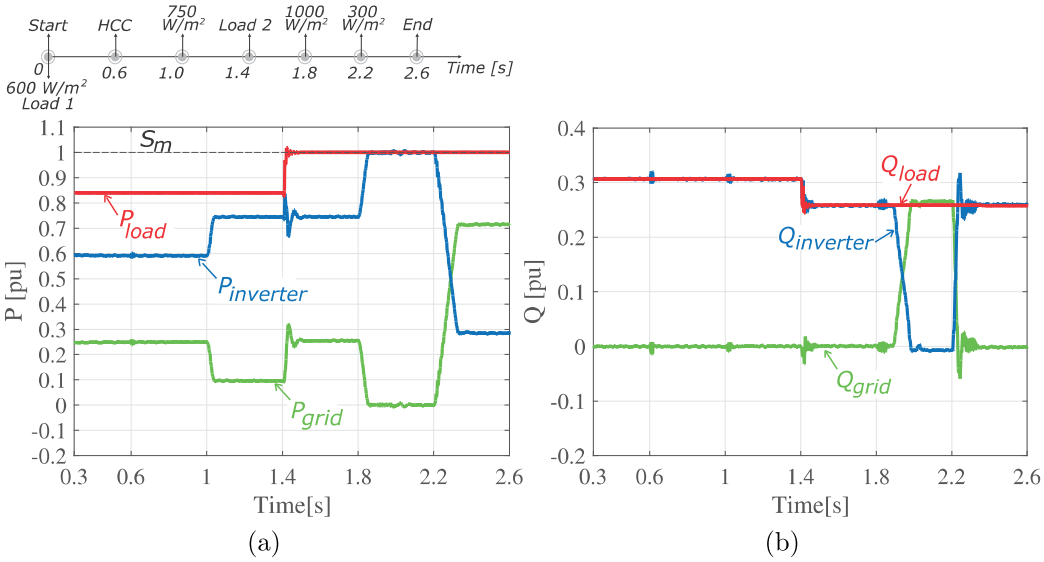

(a) (b)

Figure 4.10: Dynamic of the active power (P) and reactive power (Q) flow on the system. (a) Active power. (b) Reactive power.

The detected harmonic current is analyzed by the inverter current limitation techniques in order to determine if the harmonic current compensation will be partial or total. Fig. 4.11 shows the harmonic compensation factor K_h calculated for both techniques addressed in this work, the open-loop based method and closed-loop based method. It is possible to observe the similarity between the two techniques in steady-state. When the harmonic current compensation (HCC) is enabled at $t = 0.6$ seconds, the PV inverter has current margin to compensate all harmonic current ($K_h = 1$). Due to increased solar irradiance at $t = 1$ second, the factor K_h is approximately 0.80. Therefore, 80 % of the load harmonic current is compensated. At $t = 1.4$ seconds, the PV inverter has current margin to compensate only 37 % of the harmonic current of the load 2. At $t = 1.8$ seconds, the harmonic compensation is null ($K_h = 0$), under such condition, the PV inverter injects the nominal active power. After $t = 2.2$ seconds, the harmonic current compensation is total ($K_h = 1$).

Fig. 4.12 shows the inverter current waveform details during transient

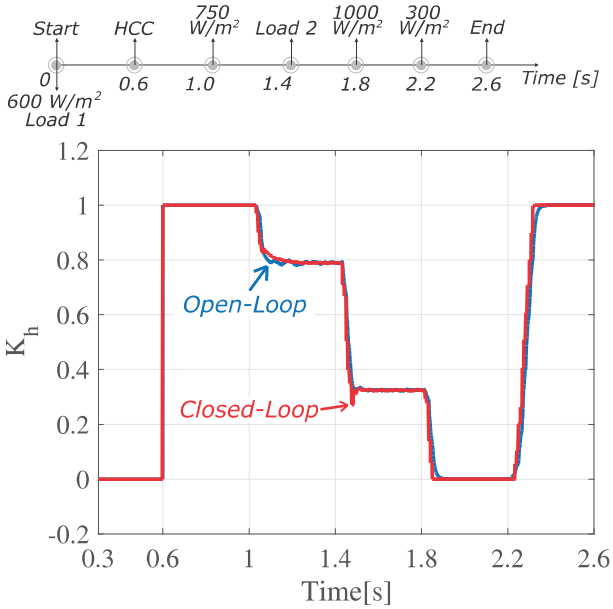

Figure 4.11: Compensation factor K_h using two techniques for inverter current limitation.

responses. At $t = 0.6$ seconds, the current waveform becomes more distorted once the harmonic current compensation starts and $K_h = 1$. At $t = 1.8$ seconds, there are no harmonic components in the inverter current because harmonic current compensation is not feasible, once the inverter injects the nominal active. It is possible to observe that the inverter current does not exceed the inverter rated current (I_m^*) in steady-state due to factor K_h activity.

The improvement in grid current quality with HCC is better noticed through the total demand distortion (TDD) index, as shown in Table 4.1. This table presents the inverter and grid current TDD in each time interval. At the beginning, the harmonic current compensation is disabled and the grid current TDD is 15.43 %, while the inverter injects only the fundamental current component and thus the inverter current TDD is 1.64 %. At $t = 0.6$ seconds, the HCC starts and the grid current TDD becomes 3.87 %. The worst case is between $t = 1.8$ and $t = 2.2$ seconds, when the harmonic current compensation is disabled by the factor K_h. In this case, the grid current TDD is 30.97 %.

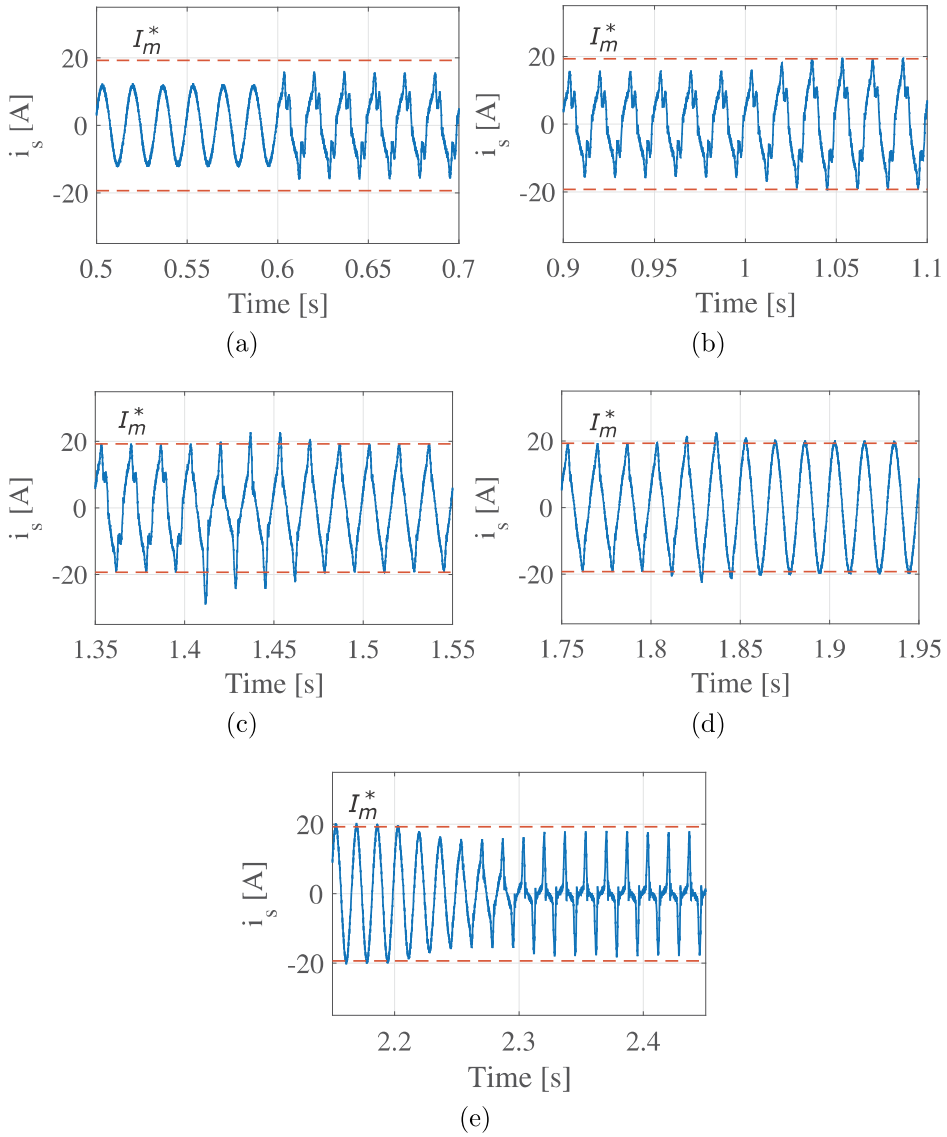

Figure 4.12: Inverter current waveform details during transient responses.(a) Transient response at 1 s. (b) Transient response at $t = 0.6$ seconds. (b) Transient response at $t = 1$ second. (c) Transient response at $t = 1.4$ seconds. (d) Transient response at $t = 1.8$ seconds. (e) Transient response at $t = 2.2$ seconds.

In order to demonstrate that the inverter current is bounded by its rated value after the factor K_h action, the space phasor of the grid current is emulated for single-phase system with and without the inverter limitation

Table 4.1: Total demand distortion of the currents.

Time interval [s]	i_s **TDD** [%]	i_g **TDD** [%]
$0 < t < 0.6$	1.64	15.43
$0.6 < t < 1.0$	15.67	3.87
$1.0 < t < 1.4$	12.33	4.74
$1.4 < t < 1.8$	10.79	20.51
$1.8 < t < 2.2$	2.43	30.97
$2.2 < t < 2.6$	32.00	3.95

technique, as shown in Fig. 4.13. For this purpose, the current quadrature component is obtained by delaying the current by 90^o. Firstly, the space phasor of the inverter current (i_s) is outside the circumference delimiting the inverter rated current (I_m^*), as shown in Fig. 4.13(a). This fact demonstrates that the PV inverter compensates the harmonic current outside its current margin. Due to K_h activity, the inverter current is placed within the maximum limit, as shown in Fig. 4.13(b).

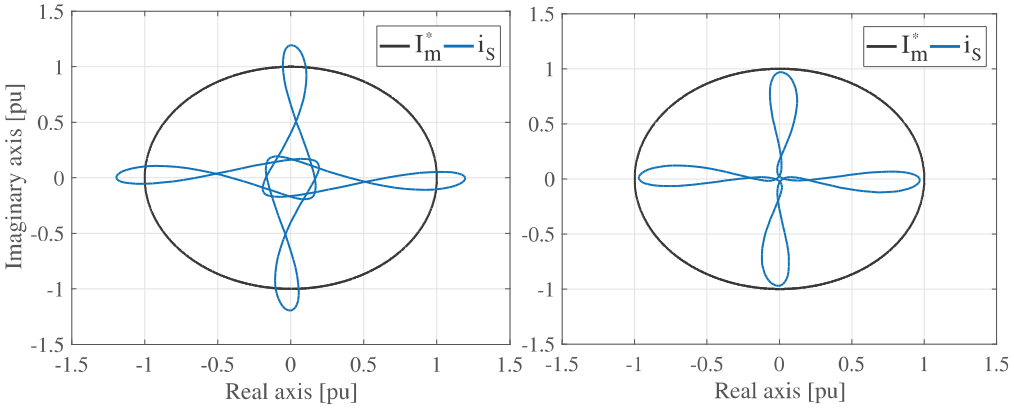

Figure 4.13: Inverter current space phasor. (a) Without harmonic current limitation technique. (b) With harmonic current limitation technique.

A simulation case study was performed in order to validate the techniques for partial harmonic current compensation proposed in this work. It can be seen that even by injecting active and reactive power most of the time, the PV inverter can help to reduce harmonic distortions in the grid current in several moments and always respecting its current capacity.

4.4 Experimental Results

A case study in experimental environment is shown in order to validate the techniques for partial harmonic current compensation proposed in this work. The experimental prototype of this case study is the same described in 3.3.

In order to test these techniques under high levels of harmonic distortions in the inverter current, all multiple odd harmonics of the fundamental frequency until the 15th harmonic order are compensated. The load current in this case study is held constant and its spectrum is shown in Fig. 3.19(b).

The case study starts when the inverter injects no fundamental current ($i_f = 0$) and when the harmonic current compensation (HCC) is enabled. Next, the amplitude of the fundamental current component injected by the inverter is increased by 6 A every 1.5 seconds. Both the inverter rated current (I_m^*) and the maximum demand PCC current at the fundamental frequency used in the TDD calculation is set to 18 A.

Fig. 4.14 shows the harmonic compensation factor in experimental environment for both techniques addressed in this work. At the beginning of the experiment the PV inverter has current margin to compensate all harmonic current, i.e., $K_h = 1$. Due to the increase in the injected fundamental current at $t = 1.5$ seconds to 6 A, the factor K_h is around 0.8, approximately. Therefore, partial harmonic current compensation is performed from this instant. At $3 < t < 4.5$ seconds, the injected fundamental current is increased again to 12 A and 18 A, respectively. The factor K_h decreases to around 0.4 and zero, respectively. Therefore, PV inverter ceases the harmonic current compensation.

Fig. 4.15 shows current waveforms and spectra of the load, inverter and grid during harmonic compensation with inverter current limitation technique based on the open-loop technique. At the beginning, the harmonic compensation is total ($K_h = 1$) and no fundamental current is injected, which simulates the low solar irradiance condition and no reactive power injection service. Therefore, Fig. 4.15(a) shows high grid current quality. Almost all load harmonic currents are supplied by the PV inverter and the grid current is very close to a sinusoidal signal. The grid current TDD is 3.82 %. Note

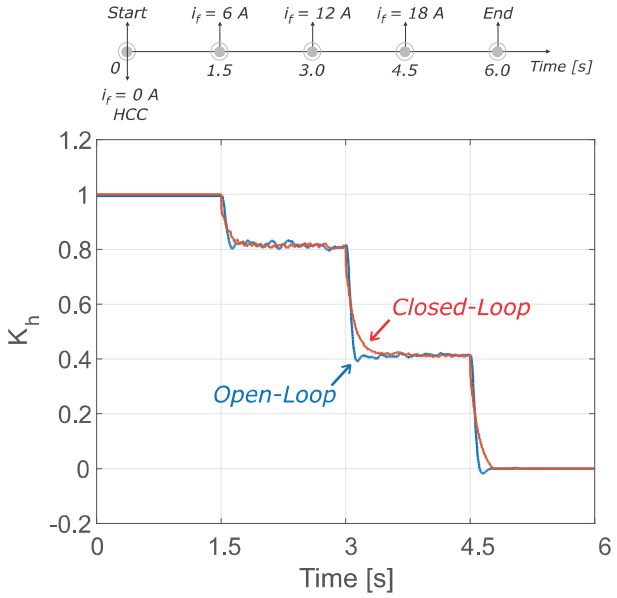

Figure 4.14: Experimental compensation factor K_h using two techniques for inverter current limitation.

that, without harmonic current compensation, the grid current TDD would be equal to the load current TDD of 50.34%.

At $t = 1.5$ seconds, the PV inverter injects 6 A of fundamental current. Under such conditions, the inverter partially compensates the harmonic current ($K_h = 0.8$). Thus, there is a small distortion in the grid current and its TDD is 8.82 %, as shown in Fig. 4.15(b). At $t = 3$ seconds, the PV inverter injects 12 A of fundamental current. In this case, the grid current waveform distortion is more evident, as shown in Fig. 4.15(c). The TDD of this current is 29.33 %. At $t = 4.5$ seconds, the PV inverter injects 18 A of fundamental current, which is the rated current of this device. For this reason, the harmonic current compensation is disabled by the factor $K_h = 0$. The grid current waveform presents a high distortion index and its TDD is equal to 49.07 %, as shown in Fig. 4.15(d).

The current waveforms and spectra are also presented for a case study using the inverter current limitation based on the closed-loop technique, as shown in Fig. 4.16. It can be seen that this technique and the open-loop technique have similar results, with small differences in the TDD of the grid and inverter current. These differences are due to the grid voltage quality

variation between the tests, which slightly changes the load harmonic current content.

In relation to the computational burden, the closed-loop technique for inverter current limitation presents an execution time of 2.68 μs to calculate and update the factor K_h. The open-loop technique is executed in 4.24 μs by the digital signal processor to calculate and update the factor K_h. This execution time is accomplished when the relation shown in (4.1) is required, which may occur at the end of each fundamental frequency cycle. Observed that both techniques have a low execution time but the closed-loop technique runs faster than the open-loop technique. The relation (4.1) is responsible for increasing the computation burden of the open-loop technique.

An experimental case study was performed in order to validate the methodology for harmonic current limitation based on a open-loop and a close-loop technique. It was possible to verify the similarity of the two techniques in steady state and the high quality improvement of the grid current when the PV inverter has current margin to provide harmonic current compensation. As can be seen that the inverter rated current (18 A) is never exceed in any moment in steady state, ensuring the safe operation of this device.

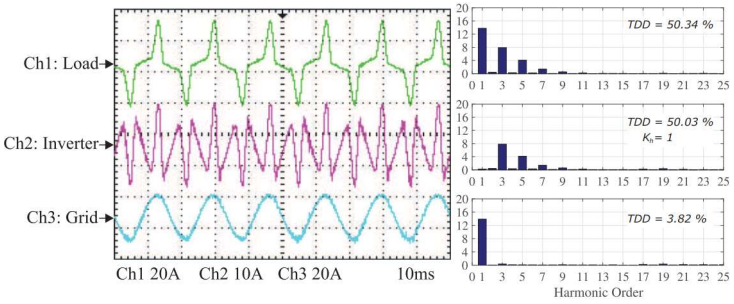

(a)

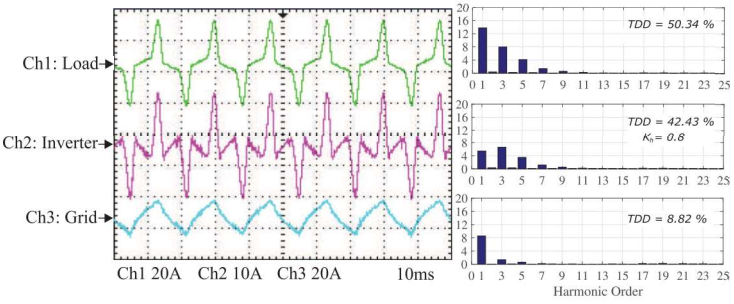

(b)

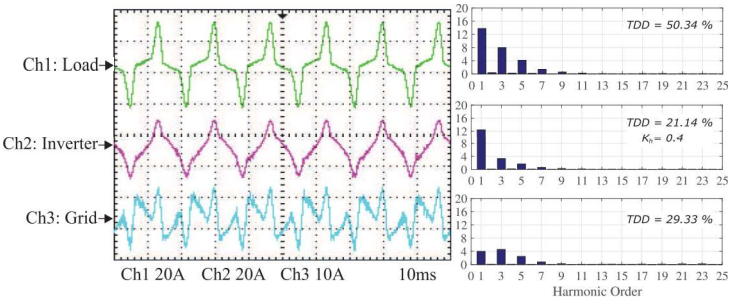

(c)

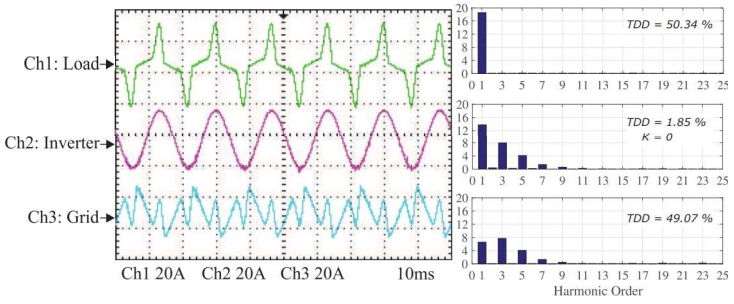

(d)

Figure 4.15: Current waveforms and spectra of the system during harmonic compensation with inverter current limitation based on open-loop technique. (a) $0 < t < 1.5$ seconds. (b) $1.5 < t < 3.0$ seconds. (c) $3.0 < t < 4.5$ seconds. (d) $4.5 < t < 6$ seconds.

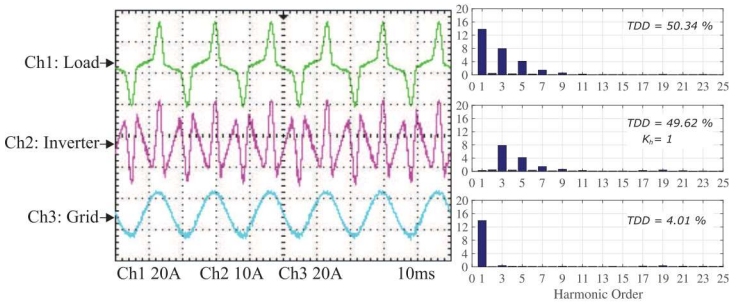

(a)

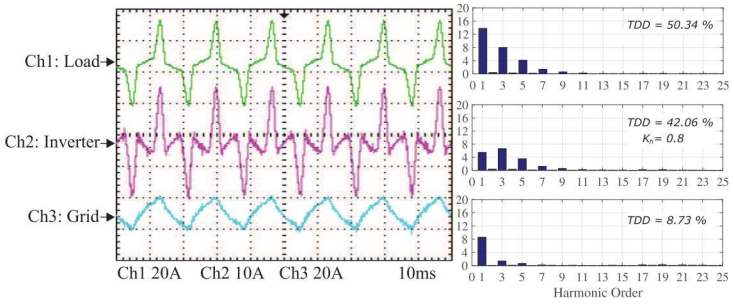

(b)

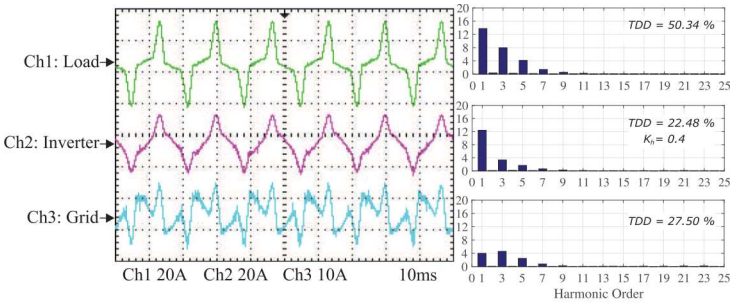

(c)

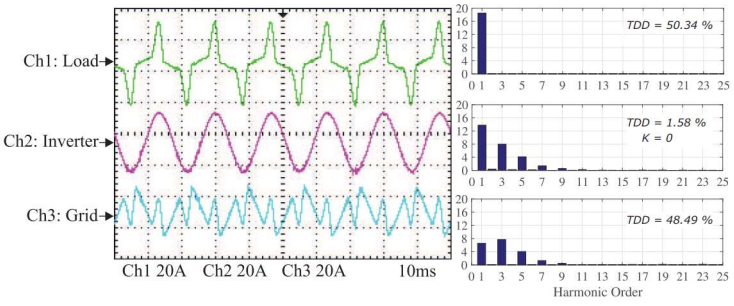

(d)

Figure 4.16: Current waveforms and spectra of the system during harmonic compensation with inverter current limitation based on closed-loop technique. (a) $0 < t < 1.5$ seconds. (b) $1.5 < t < 3.0$ seconds. (c) $3.0 < t < 4.5$ seconds. (d) $4.5 < t < 6$ seconds.

Chapter 5

Conclusions

This work presented a single-phase photovoltaic system connected to the power grid with capability to perform ancillary services such as reactive power injection and harmonic current compensation. These capabilities supports the electrical power system under high connections of nonlinear loads and demanding reactive power, for example.

A harmonic current detection method applied in single-phase photovoltaic inverters for selective harmonic current compensation was developed in this work. This strategy was designed to extract the predominant harmonics in a distorted current. In addition, the frequencies of each predominant harmonic component were detected and then the proportional multiple resonant current controller can be automatically tuned for specific harmonics, increasing the controller signal tracking capability. Analysis of the current harmonic detector and the effect of the algorithm parameters were addressed.

Furthermore, two techniques to limit the peak value of the inverter current for partial harmonic current compensation were proposed. One technique based on the closed-loop control and other based on open-loop method. This work proved that the two techniques are very similar in steady state response. The partial harmonic current have proved to be very important ensuring that the inverter works in a safe operation mode in terms of the current peak passing through the power switches.

Simulation and experimental results show the performance of the proposed strategies and improvements in the grid current quality. The total demand distortion (TDD) is reduced through harmonic current compensation of the nonlinear loads connected to the PCC, using the photovoltaic

inverter.

In such conditions, if several photovoltaic systems are already installed into the power system, the modifications in the control strategy for partial harmonic compensation can result in considerable improvement in the grid power quality.

5.1 Future Works

As continuity of this work can be cited:

- It may seem consensus that inserting other services in the photovoltaic system can reduce the lifetime of the PV inverter. Therefore, studies about the inverter prediction lifetime during operation with ancillary services need to carried out and compared with the lifetime in normal operation (injecting the PV energy in the grid).
- Inverter thermal analysis with harmonic current limitation strategies proposed here.
- Implement the strategies proposed here in a complete PV system, with PV panels and DC/DC stage.
- Develop a strategy to limit the harmonic compensation in accordance to the DC-link voltage.

References

ABINEE. *Propostas para Inserção da Energia Solar Fotovoltaica na Matriz Eletrica Brasileira*. [S.l.], 2012.

AKAGI, H.; KANAZAWA, Y.; NABAE, A. Instantaneous reactive power compensators comprising switching devices without energy storage components. *IEEE Transactions on Industry Applications*, IA-20, n. 3, p. 625–630, May 1984.

ANEEL. Resolução Normativa n 482. *Aneel*, p. 9, 2012. ISSN 1098-6596.

ANEEL. Nota Técnica n 0056/2017-SRD/ANEEL: Atualização das projeções de consumidores residenciais e comerciais com microgeração solar fotovoltaicos no horizonte 2017-2024. *Agência Nacional de Energia Elétrica*, 2017.

ANEEL. *BIG - Banco de Informações de Geração*. 2018. <http://www2.aneel.gov.br/aplicacoes/capacidadebrasil/capacidadebrasil.cfm>. Accessed on 10/05/2018.

ASIMINOAEI, L.; BLAABJERG, F.; HANSEN, S. Evaluation of harmonic detection methods for active power filter applications. In: *Twentieth Annual IEEE Applied Power Electronics Conference and Exposition, 2005. APEC 2005.* [S.l.: s.n.], 2005. v. 1, p. 635–641 Vol. 1.

BEST, R. E. *Phase-locked Loops: Design, Simulation, and Applications*. 5th. ed. New York: McGraw-Hill Professional, 2003. 421 p.

BLAABJERG, F.; TEODORESCU, R.; LISERRE, M.; TIMBUS, A. V. Overview of control and grid synchronization for distributed power generation systems. *IEEE Transactions on Industrial Electronics*, v. 53, n. 5, p. 1398–1409, 2006.

BONALDO, J. P.; PAREDES, H. K. M.; POMILIO, J. A. Control of Single-Phase Power Converters Connected to Low Voltage Distorted Power Systems with Variable Compensation Objectives. *IEEE Transactions on Power Electronics*, v. 31, n. 3, p. 2039–2052, 2016.

CAGNANO, A.; MEMBER, S. S.; TUGLIE, E. D.; LISERRE, M.; MASTROMAURO, R. a.; De Tuglie, E. Online Optimal Reactive Power Control Strategy of PV Inverters. *IEEE Transactions on Industrial Electronics*, v. 58, n. 10, p. 4549–4558, 2011.

CEMIG. *HISTÓRIA DA ELETRICIDADE NO BRASIL*. 2012. <http://www.cemig.com.br/pt-br/a_cemig/Nossa_Historia/Paginas/historia_da_eletricidade_no_brasil.aspx>. Accessed on 23/01/2018.

CIOBOTARU, M.; TEODORESCU, R.; BLAABJERG, F. A new single-phase PLL structure based on second order generalized integrator. *PESC Record - IEEE Annual Power Electronics Specialists Conference*, 2006.

CUPERTINO, A. F.; CARLETTE, L. P.; PEREZ, F.; RESENDE, J. T.; SELEME, S. I.; PEREIRA, H. A. Use of control based on passivity to mitigate the harmonic distortion level of inverters. In: *Innovative Smart Grid Technologies Latin America (ISGT LA), 2013 IEEE PES Conference On*. [S.l.: s.n.], 2013.

De la Rosa, F. C. *Harmonics and Power Systems*. Boca Raton: CRC Press Taylor & Francis Group, 2006.

ERICKSON, R. W.; MAKSIMOVIC, D. *Fundamentals of Power Electronics*. [S.l.]: Springer Science & Business Media, 2001.

GAJANAYAKE, C. J.; VILATHGAMUWA, D. M.; LOH, P. C.; TEODORESCU, R.; BLAABJERG, F. Z-source-inverter-based flexible distributed generation system solution for grid power quality improvement. *IEEE Transactions on Energy Conversion*, v. 24, n. 3, p. 695–704, Sept 2009.

GARDNER, F. *Phaselock Techniques*. 3rd. ed. Hoboken, NJ: John Wiley & Sons, 2005. 425 p.

GOLESTAN, S.; GUERRERO, J. M. Conventional synchronous reference frame phase-locked loop is an adaptive complex filter. *IEEE Transactions on Industrial Electronics*, v. 62, n. 3, p. 1679–1682, 2015.

GONZALEZ, S. A.; GARCIA-RETEGUI, R.; BENEDETTI, M. Harmonic computation technique suitable for active power filters. *IEEE Transactions on Industrial Electronics*, v. 54, n. 5, p. 2791–2796, Oct 2007.

GREEN, M. A.; HISHIKAWA, Y.; DUNLOP, E. D.; LEVI, D. H.; HOHL-EBINGER, J.; HO-BAILLIE, A. W. Solar cell efficiency tables (version 51). *Progress in Photovoltaics: Research and Applications*, v. 26, n. 1, p. 12, 2018.

HE, J.; LI, Y. W.; MUNIR, M. S. A flexible harmonic control approach through voltage-controlled dg-grid interfacing converters. *IEEE Transactions on Industrial Electronics*, v. 59, n. 1, p. 444–455, Jan 2012.

HUSSEIN, K. H.; MUTA, I.; HOSHINO, T.; OSAKADA, M. Maximum photovoltaic power tracking: an algorithm for rapidly changing atmospheric conditions. *Generation, Transmission and Distribution, IEE Proceedings-*, v. 142, n. 1, p. 59–64, jan 1995.

JOOS, G.; OOI, B. T.; MCGILLIS, D.; GALIANA, F. D.; MARCEAU, R. The potential of distributed generation to provide ancillary services. In: *2000 Power Engineering Society Summer Meeting (Cat. No.00CH37134)*. [S.l.: s.n.], 2000. v. 3, p. 1762–1767 vol. 3.

KAURA, V.; BLASKO, V. Operation of a phase locked loop system under distorted utility conditions. *IEEE Transactions on Industry Applications*, v. 33, n. 1, p. 58–63, 1997.

KEREKES, T.; TEODORESCU, R.; LISERRE, M.; KLUMPNER, C.; SUMNER, M. Evaluation of three-phase transformerless photovoltaic inverter topologies. *IEEE Transactions on Power Electronics*, v. 24, n. 9, p. 2202–2211, 2009.

KJAER, S. B.; PEDERSEN, J. K.; BLAABJERG, F. A review of single-phase grid-connected inverters for photovoltaic modules. *IEEE Transactions on Industry Applications*, v. 41, n. 5, p. 1292–1306, 2005.

LASCU, C.; ASIMINOAEI, L.; BOLDEA, I.; BLAABJERG, F. Frequency response analysis of current controllers for selective harmonic compensation in active power filters. *IEEE Transactions on Industrial Electronics*, v. 56, n. 2, p. 337–347, Feb 2009.

MASTROMAURO, R. A.; LISERRE, M.; KEREKES, T.; DELL'AQUILA, A. A single-phase voltage-controlled grid-connected photovoltaic system

with power quality conditioner functionality. *IEEE Transactions on Industrial Electronics*, v. 56, n. 11, p. 4436–4444, 2009.

MCGRATH, B. P.; HOLMES, D. G.; GALLOWAY, J. J. H. Power converter line synchronization using a discrete fourier transform (dft) based on a variable sample rate. *IEEE Transactions on Power Electronics*, v. 20, n. 4, p. 877–884, July 2005.

MIÑAMBRES-MARCOS, V.; GUERRERO-MARTÍNEZ, M. Á.; ROMERO-CADAVAL, E.; GONZÁLEZ-CASTRILLO, P. Grid-connected photovoltaic power plants for helping node voltage regulation. *IET Renew. Power Gener.*, v. 9, n. 3, p. 236–244, 2015.

MORRIS, C.; PEHNT, M. Energy Transition, The German Energiewende. *Energy Transition*, p. 112, 2012.

PAREDES, H. K. M.; BRANDAO, D. I.; TERRAZAS, T. M.; MARAFAO, F. P. Shunt active compensation based on the Conservative Power Theory current's decomposition. In: *XI Brazilian Power Electronics Conference (COBEP)*. [S.l.: s.n.], 2011. p. 788–794.

PAREDES, H. K. M.; MARAFÃO, F. P.; BRANDÃO, D. I.; COSTABEBER, A. Multi-task control strategy for grid-tied inverters based on conservative power theory. *IET Renewable Power Generation*, v. 9, n. 2, p. 154–165, 2015.

PEÑA-ALZOLA, R.; LISERRE, M.; BLAABJERG, F.; ORDONEZ, M.; YANG, Y. LCL-filter design for robust active damping in grid-connected converters. *IEEE Transactions on Industrial Informatics*, v. 10, n. 4, p. 2192–2203, 2014.

PEPERMANS, G.; DRIESEN, J.; HAESELDONCKX, D.; BELMANS, R.; D'HAESELEER, W. Distributed generation: Definition, benefits and issues. *Energy Policy*, v. 33, n. 6, p. 787–798, 2005.

PEREIRA, H. A.; XAVIER, L. S.; CUPERTINO, A. F.; MENDES, V. F. Single-phase multifunctional inverter with dynamic saturation scheme for partial compensation of reactive power and harmonics. In: *2015 17th European Conference on Power Electronics and Applications (EPE'15 ECCE-Europe)*. [S.l.: s.n.], 2015.

PINHO, J. T.; GALDINO, M. A. Manual de Engenharia para Sistemas Fotovoltaicos. *CEPEL CRESESB*, 2014.

PINTO, H. S.; FARIA, I. D.; BAPTISTA, R.; KASSMAYER, K.; ABBUD, A.; PINTO, V. C. A Crise Hídrica e suas Consequências. *Núcleo de estudo e pesquisas - Senado Federal*, p. 1–32, 2015.

RAUSCHENBACH, H. S. *Solar Cell Array Design Handbook: The Principles and Technology of Photovoltaic Energy Conversion*. New York: Van Nostrand Reinhold, 1980. 549 p.

REN21. *Renewables 2017: global status report*. [S.l.: s.n.], 2017. v. 72.

RODRIGUEZ, P.; LUNA, A.; CANDELA, I.; MUJAL, R.; TEODORESCU, R.; BLAABJERG, F. Multiresonant frequency-locked loop for grid synchronization of power converters under distorted grid conditions. *IEEE Transactions on Industrial Electronics*, v. 58, n. 1, p. 127–138, Jan 2011.

RYAN, M. J.; BRUMSICKLE, W. E.; LORENZ, R. D. Control topology options for single-phase ups inverters. *IEEE Transactions on Industry Applications*, v. 33, n. 2, p. 493–501, Mar 1997.

SEMIKRON. *Power Electronic System - SEMISTACK*. 2006. <https://www.semikron.com/>. Accessed on 05/04/2018.

SERA, D.; TEODORESCU, R.; HANTSCHEL, J.; KNOLL, M. Optimized Maximum Power Point Tracker for Fast-Changing Environmental Conditions. *IEEE Transactions on Industrial Electronics*, v. 55, n. 7, p. 2629–2637, 2008.

TEODORESCU, R.; LISERRE, M.; RODRIGUEZ, P. *Grid Converters for Photovoltaic and Wind Power Systems*. [S.l.]: Wiley-IEEE Press, 2011.

TUMMURU, N. R.; MISHRA, M. K.; SRINIVAS, S. Multifunctional vsc controlled microgrid using instantaneous symmetrical components theory. *IEEE Transactions on Sustainable Energy*, v. 5, n. 1, p. 313–322, Jan 2014.

VILLALVA, M. G.; GAZOLI, J. R.; FILHO, E. R. Comprehensive Approach to Modeling and Simulation of Photovoltaic Arrays. *Power Electronics, IEEE Transactions on*, v. 24, n. 5, p. 1198–1208, 2009.

VILLALVA, M. G. G.; SIQUEIRA, T. G. G. de; RUPPERT, E. Voltage regulation of photovoltaic arrays: small-signal analysis and control design. *IET Power Electronics*, v. 3, n. 6, p. 869, 2010.

WATANABE, E. H.; AKAGI, H.; AREDES, M. Instantaneous p-q power theory for compensating nonsinusoidal systems. In: *2008 International*

School on Nonsinusoidal Currents and Compensation. [S.l.: s.n.], 2008. p. 1–10.

XAVIER, L. S.; CUPERTINO, A. F.; PEREIRA, H. A. Adaptive saturation scheme for a multifunctional single-phase photovoltaic inverter. In: *IEEE/IAS International Conference on Industry Applications*. [S.l.: s.n.], 2014. p. 1–8.

XAVIER, L. S.; CUPERTINO, A. F.; RESENDE, J. T. de; MENDES, V. F.; PEREIRA, H. A. Adaptive current control strategy for harmonic compensation in single-phase solar inverters. *Electric Power Systems Research*, Elsevier B.V., v. 142, p. 84–95, 2017.

YANG, Y. *Advanced Control Strategies to Enable a More Wide-Scale Adoption of Single-Phase Photovoltaic Systems*. 150 p. Tese (Doutorado) — Aalborg University, 2014.

YANG, Y.; WANG, H.; BLAABJERG, F. Reactive Power Injection Strategies for Single-Phase Photovoltaic Systems Considering Grid Requirements. *IEEE Trans. Ind. Appl.*, v. 50, n. 6, p. 4065–4076, 2014.

YANG, Y.; ZHOU, K.; BLAABJERG, F. Frequency adaptability of harmonics controllers for grid-interfaced converters. *International Journal of Control*, v. 90, n. 1, p. 3–14, 2015.

YAZDANI, A.; IRAVANI, R. *Voltage-Sourced Converters in Power Systems: Modeling, Control, and Applications*. [S.l.]: Wiley-IEEE Press, 2010. 541 p.

YEPES, A. G.; FREIJEDO, F. D.; DOVAL-GANDOY, J.; LÓPEZ, Ó.; MALVAR, J.; FERNANDEZ-COMESAÑA, P. Effects of Discretization Methods on the Performance of Resonant Controllers. *IEEE Trans. Power Electron.*, v. 25, n. 7, p. 1692–1712, 2010.

YEPES, A. G.; FREIJEDO, F. D.; LOPEZ, O.; DOVAL-GANDOY, J. Analysis and Design of Resonant Current Controllers for Voltage-Source Converters by Means of Nyquist Diagrams and Sensitivity Function. *IEEE Transactions on Industrial Electronics*, v. 58, n. 11, p. 5231–5250, 2011.